CrossMark

JM PAPERS

Vortex-to-velocity reconstruction for wall-bounded turbulence via the field-based linear stochastic estimation

Chengyue Wang[1,3], Qi Gao[2,3,†], Biao Wang[1,†], Chong Pan[3] and Jinjun Wang[3]

[1]Sino-French Institute of Nuclear Engineering and Technology, Sun Yat-sen University, Zhuhai 519082, PR China

[2]School of Aeronautics and Astronautics, Zhejiang University, Hangzhou 310027, PR China

[3]Fluid Mechanics Key Laboratory of Education Ministry, Beijing University of Aeronautics and Astronautics, Beijing 100191, PR China

Representing complex flows by evolving vortex structures is an important principle in many investigations of wall-bounded turbulence. The practice of this principle benefits from the bi-directional transformation between the velocity field and the corresponding vortex field. While the velocity-to-vortex transformation could be implemented by various vortex identification criteria, few efforts have been devoted to the inverse process. This work develops a linear reconstruction method, which allows an effective reconstruction for the velocity field of wall turbulence based on a given vortex field. The vortex field is defined as a vector field by combining the swirl strength and the real eigenvector of the velocity gradient tensor. The reconstructed velocity fields are calculated by convolution operations on the vortex fields, with the kernel functions derived by the field-based linear stochastic estimation. The method can effectively recover the turbulent motions in a large scale range, showing clear advantages over the Biot–Savart formula in the near-wall region. The method is also employed to investigate the inducing effects of vortices at different heights. The wall-bounding effect on the induced motions is observed from the contribution spectra of vortices. The higher-order moments of the reconstructed streamwise velocity component present larger deviations from the original data, which is discussed and explained reasonably. At last, the vortex fields filtered by prescribed thresholds are employed to reconstruct the velocity fields. It is found that the strongest vortex components occupying 5 % of the total volume can reasonably recover the main flow features including both the near-wall streaks and the large-scale motions.

Key words: boundary layer structure, turbulent boundary layers, vortex dynamics

† Email addresses for correspondence: qigao@zju.edu.cn, wangbiao@mail.sysu.edu.cn

1. Introduction

The concept of vortex is of prime importance in revealing the underlying physics behind complex flows. In wall-bounded turbulence, the roles of vortices have been emphasized by extensive research works. In various self-sustaining mechanisms as reviewed by Panton (2001), quasi-streamwise vortices are closely linked to the low-speed streaks populated in the buffer layer (Hama 1954; Kline *et al.* 1967), which is vital for the autonomous cycle of near-wall turbulence (Einstein & Li 1958; Jiménez & Pinelli 1999; Bandyopadhyay & Hellum 2014). On the other hand, investigation works focusing on the outer layer provide accumulated evidence that the hairpin vortices (Theodorsen 1952; Head & Bandyopadhyay 1981) and their well-organized packets (Adrian, Meinhart & Tomkins 2000) are the building blocks of large-scale motions.

A number of investigators are devoted to the study on the characteristics of vortices in wall-bounded turbulence. Usually, these vortices were recognized from velocity fields based on certain identification criteria (Chakraborty, Balachandar & Adrian 2005). Tanahashi and his coworkers (Tanahashi *et al.* 2004; Das *et al.* 2006; Kang, Tanahashi & Miyauchi 2007) extensively investigated the properties of the tube-like vortices (termed coherent fine-scale eddies, CFSEs) based on the direct numerical simulations (DNSs) of turbulent channel flows. When normalized by local Kolmogorov scale (η) and the root mean square of velocity fluctuations (u_{rms}), the diameter and the maximum azimuthal velocity for CFSEs are 10–12η and 0.5–$0.6u_{rms}$ respectively, independent of the wall-normal positions and Reynolds numbers (Das *et al.* 2006). The universal scaling laws gained further supported by the DNS of turbulent channel flow at a higher friction Reynolds number ($Re_\tau = 1900$) (del Álamo *et al.* 2006), and by the particle image velocimetry (PIV) of the turbulent boundary flows for Re_τ up to 6868 (Stanislas, Perret & Foucaut 2008; Herpin *et al.* 2013). Herpin *et al.* (2013) took into account for the orientation of vortices by conducting stereo PIVs in both the streamwise–wall-normal plane and the spanwise-wall-normal plane. They found that the probability density functions (p.d.f.s) of the vortex radius and the vorticity in the logarithmic layer can be fitted by a log-normal distribution in good qualities, and the fitting parameters show remarkably independent of Reynolds numbers.

Orientation is another aspect of vortex characteristics, which implies the elongating direction of vortex tubes and offers useful information to infer the topologies of dominant vortex structures. Ong & Wallace (1998), Ganapathisubramani, Longmire & Marusic (2006) and Kang *et al.* (2007) inferred the vortex orientation based on the inclination angles of vorticity vectors. One widely cited result is that the vortex structures at the logarithmic layer tend to incline at an angle of 45° with respect to the streamwise direction, which was theoretically explained by Head & Bandyopadhyay (1981). Bandyopadhyay (1980) conjectured that the upstream interface of large-scale motions consists of an array of 45°-inclined hairpin vortices with respect to the streamwise direction and derived the interface slope angle is 18.4°, consistent with the previous experimental observations. Against the use of vorticity direction as the vortex orientation, Bernard, Thomas & Handler (1993) and Gao, Ortiz-Dueñas & Longmire (2007) argued that the local vorticity vector tends to be deflected away from the vortex axis at locations very close to the wall. Zhou (1997) demonstrated that the real eigenvector (Λ_r) of the velocity gradient tensor is well aligned with the vortex axis by tracking Λ_r within a hairpin vortex. Using Λ_r as the indicator for vortex orientation, Gao, Ortiz-Dueñas & Longmire (2011) refined the vortex characteristics including orientations, circulation, propagation velocities at three different wall-parallel planes. Recently, Tian *et al.* (2018) proposed a new definition for the orientation of vortex based on the coordinate transformation, which turned out to be Λ_r (Gao & Liu 2018). Also based on Λ_r criterion, Wang *et al.* (2019) extended the work of

Gao *et al.* (2011) and offered full information of vortex orientation, shapes and organizations for larger Reynolds-number range ($Re_\tau = 1238 \sim 3081$) based on tomographic PIV data and DNS data.

Besides aforementioned works regarding general vortices, there are also a lot of investigations focusing on the vortices with specific geometries for the modelling purpose, such as the hairpin vortices, packets or attached vortex structures. Christensen & Adrian (2001) statistically investigated the geometrical characteristics of packets structures in the streamwise–wall-normal plane, and found their streamwise inclination angle with respect to the wall is 12°–13°. Wu & Christensen (2006) investigated the population trends of prograde and retrograde spanwise vortices in wall turbulence. Natrajan, Wu & Christensen (2007) recognized the pairing trend of prograde and retrograde vortices and interpreted the vortex pairing as the signature of a Ω-shape vortex. Deng *et al.* (2018) filtered out the spanwise vortices not aligned in a packet based on proper orthogonal decomposition and discovered a $Re_\tau^{1/2}$ scaling of the saturated streamwise spacing between two hairpin heads in one packet. Besides these PIV measurements limited in the streamwise–wall-normal plane, Ganapathisubramani, Longmire & Marusic (2003) recognized the patterns of vortex packets in the streamwise–spanwise plane and estimated that these patterns contribute more than 25 % to the total Reynolds stress while occupying only 5 % of the total area in the logarithmic layer. Hutchins, Hambleton & Marusic (2005) investigated the patterns of hairpin packets in the 135°-inclined plane with respect to the streamwise direction and found distinct two-regime behaviours: attached to the wall and detached from it, with a demarcation scaled well with the outer variables. The attached and detached structures were also reported by del Álamo *et al.* (2006), who recognized tall attached vortex clusters and detached vortex clusters based on three-dimensional (3-D) DNS data of turbulent channel flow. They found that the attached eddies are self-similar with a constant height–width–length of 1 : 1.5 : 3 while the sizes of detached eddies are proportional to the local Kolmogorov scale.

These investigations involve the statistical information about the size, intensity, orientation and organizations of vortices in wall-bounded turbulence, which add to the understanding of the wall-turbulence structures and also provide valuable materials for the modelling works. The hairpin model and the attached eddy model are two well-known models in the wall-turbulence community. The hairpin model, first proposed by Theodorsen (1952), gained renewed interest after the experimental investigations of Bandyopadhyay (1980) and Head & Bandyopadhyay (1981). Adrian (2007) extended the hairpin model by invoking the packet features found by PIV, and put forward a conceptual multi-hairpin paradigm to explain many observations in wall turbulence. The attached eddy model was proposed by Townsend (1956), which provided a theoretical framework to predict the flow statistics in the logarithmic region. Perry and his coworkers (Perry & Chong 1982; Perry, Henbest & Chong 1986; Marusic & Perry 1995; Perry & Marusic 1995) advanced the attached eddy model by using a hairpin-shape vortex skeleton as the attached eddy candidate, and gave a recipe for inferring the turbulence intensity distributions and the turbulence spectra. More recently, the attached eddy theory has achieved vast success in predicting the statistics (Woodcock & Marusic 2015; Yang, Marusic & Meneveau 2016) and in recovering the instantaneous flow features, including the uniform momentum zone (de Silva, Hutchins & Marusic 2016*a*) and large coherence structures of spanwise velocities (de Silva *et al.* 2018). Marusic & Monty (2019) reviewed the past research works and discussed underlying assumptions for the attached eddy model.

The hairpin model and the attached eddy model share the same notion that the chaotic and multiscale wall turbulence can be represented by a collection of more

elementary structures. These elementary structures could be typical vortex models obtained by averaging many instantaneous vortex structures in wall turbulence. These aforementioned investigations regarding vortex characteristics provide references for refining the geometry of the vortex model. Once the vortex geometry is specified, a translation from vortex to velocity is necessary, which is termed as the vortex-to-velocity (V2V) reconstruction in the present work. Perry & Marusic (1995) formulated a Gaussian distribution of vorticity in the vortex cores, with the vorticity orientation consistent with the vortex axis. Subsequently, they employed the well-known Biot–Savart law to reconstruct the velocity field in the logarithmic region. It was assumed that the vorticity is concentrated inside the vortex cores and the surrounding flows could be regarded as irrotational (Perry & Chong 1982). Nevertheless, for the buffer layer, the surrounding vorticity cannot be neglected due to the stronger viscosity effect. Besides, the vorticity direction could also deviate from the vortex orientation (Wang *et al.* 2019). Extending application range for the vortex model to the buffer region will pose new challenges for the V2V reconstruction, which necessitates new methods in place of the Biot–Savart law.

Besides the velocity reconstruction based on ideal vortex models, the reconstruction based on real instantaneous vortex fields is also beneficial for the analysis regarding the inducing effects of vortices in wall turbulence. In the investigation of Ganapathisubramani *et al.* (2003), the contribution of vortex packets to the Reynolds shear stress was estimated based on a pattern-recognized strategy. Specifically, only the low-speed streaks flanked by packets were counted in the contribution, which caused an underestimated result because the packets also induce the sweep events (high-speed zones) besides the low-speed streaks (Marusic & Adrian 2012). Recently, Berk & Ganapathisubramani (2019) employed the Biot–Savart law to derive the vortex-induced velocity when dealing with a synthetic jet issuing into a turbulent boundary layer, which highlighted the including effects of vortices. A more correlated work on canonical wall turbulence is reported by Pirozzoli, Bernardini & Grasso (2010), who compared the roles of vortex tubes and vorticity sheets (termed as vortex sheets in their article) by separately reconstructing velocity fields based on these two types of structures. A Poisson equation was solved to implement the reconstruction, which had been developed for the reconstruction regarding the intense vorticity (Jiménez *et al.* 1993). The reconstructed results based on only vortex tubes are not very organized, especially at the buffer layer compared with the results of vortex sheets. They concluded that the vorticity sheets had a more important collective effect and contributed more to the turbulence production. However, it should be pointed out that the effects of vortex tubes might be underestimated since the reconstruction method was established for the vorticity-based reconstruction.

A generalized discussion on how to reconstruct velocity fields based on given vortex fields also builds on the well-developed vortex identification methods, which remains a focus in the turbulence community up to the present day (Tian *et al.* 2018; Xiong & Yang 2019; Zhu & Xi 2019). The starting point of various vortex identification schemes is to extract tube-like vortices from complex flows, removing the influence of the surrounding shear layers in the flow. The vortex tubes are quite sparse in the spatial field and could be simply represented as 3-D curved lines with fewer adjustable parameters. The process of extracting vortices from turbulence is much like a data compression process, as pointed out by Chakraborty *et al.* (2005). V2V reconstruction is the inverse process of this compression, which decompresses the vortex representations to recover original turbulence fields. Naturally, the compression and decompression are two fundamental aspects for the vortex-representing principle of wall-bounded turbulence, yet only the former has been focused on in the previous investigations.

Motivated by these considerations, the current work will focus on the topic of the V2V reconstruction. It should be addressed that the current work mainly considers the kinematic representation of wall turbulence. The current V2V reconstruction is also different from the vorticity-based velocity reconstruction involved in the vortex method for simulating the Navier–Stokes equations (Leonard 1985; Koumoutsakos & Leonard 1995; Bernard 2013; Caprace, Winckelmans & Chatelain 2020). In those works, the velocity field is reconstructed based on the vorticity field. Basically, the intense-vorticity regions could take the forms of filaments, sheets and blobs, yet only the filament (or tube-like) elements are recognized as vortices for most situations (Marusic & Adrian 2012). The current work focuses on tubular vortices and regards them as the constructing elements of wall turbulence, which is the common spirit of many structure-based models. Perry & Chong (1987) commented that 'these vortex skeletons are the "genetic code" of the flow field, since this requires very little specification and the Biot-Savart law can be used to generate the velocity field'. Thus, we confine that the reconstruction in the current investigation should use the geometry and strength information of tubular vortices only. For convenience, a vortex field will be defined by combining the existing identification criteria for the vortex magnitude and orientation, which contain all the information required for the reconstruction.

In this work, the V2V reconstruction will be implemented by a data-driven method, termed field-based linear stochastic estimation, which is a generalized method to estimate one 3-D field based on another. Mathematically, the new method could be viewed as the least-square estimation on the linear inducing effects of vortices. The reconstruction accuracy will be estimated and compared with the Biot–Savart law. Before introducing the V2V reconstruction, the geometrical property of the vortex field will be investigated, with the purpose of showing the distinct aspect differing from the vorticity field. An interesting aspect about the relationship between vortex magnitude and orientation will be revealed based on the differential geometry, which supports the definition of the vortex vector.

The remainder of this work is arranged as follows. In § 2, the DNS data employed in this investigation and associated numerical processing techniques are introduced. In § 3, the geometrical property of the vortex field is discussed. Subsequently, the theory and implementation for the field-based linear stochastic estimation as a V2V reconstruction method are introduced in § 4. In § 5, the V2V reconstruction method is numerically validated and compared with the Biot–Savart law. The inducing effects of vortices, the limitations of the method and the roles of strong and weak vortex components are further discussed based on the reconstruction results, followed by the concluding remarks in § 6.

2. The DNS data and processing techniques

2.1. *The DNS data*

The data employed by this work came from an open-access DNS database (https://torroja.dmt.upm.es/) for high-Reynolds-number turbulent boundary layer (TBL). A full description of the algorithm and the computational set-up could be found in the papers of Simens *et al.* (2009) and Borrell, Sillero & Jiménez (2013). Basically, their simulation bypassed the transition stage for boundary layer and directly generated a developed TBL with accurate inflow conditions. The inflow for this simulation was fed by an auxiliary simulation, whose calculation domain is located at the upstream of the main simulation domain. The inflow for the auxiliary simulation was obtained from one plane in its own domain using a rescaling–recycling scheme (Lund, Wu & Squires 1998).

The DNS data (Sillero, Jiménez & Moser 2013) have been widely validated by the Jiménez group (Borrell *et al.* 2013; Sillero *et al.* 2013; Sillero, Jiménez & Moser 2014). Particularly, Sillero *et al.* (2013) showed that the skin friction and shape factor from this simulation agree well with the empirical fit of Monkewitz, Chauhan & Nagib (2007), with the mean percentage deviations less than 1 %. This indicates that the canonical asymptotic state is attained after the relaxation of the auxiliary simulation. A number of investigators (Marusic, Baars & Hutchins 2017; Wang, Wang & He 2017; Wang *et al.* 2018; Chen & Sreenivasan 2021; Wang, Pan & Wang 2021) cited the DNS dataset in their investigation works. In our previous work (Wang *et al.* 2019), we compared the DNS data with 3-D PIV data regarding several aspects, including the p.d.f. of the vortex orientation angles and the conditionally averaged vortex structures. The DNS results and the experimental results were remarkably consistent, which further emboldens us to use the DNS data.

The production DNS field corresponds to a spatially evolving zero pressure gradient TBL from $Re_\tau \approx 1000$ to $Re_\tau \approx 2000$. The calculation domain contains 15361, 4096 and 535 grid nodes for the streamwise, spanwise and wall-normal directions, respectively. The separation between adjacent collocation points along the wall-normal direction is non-uniform, which is determined by local Kolmogorov scale (Borrell *et al.* 2013). The DNS dataset is fully resolved and covers a vast scale range, which provides an ideal database for the implementation and validation of the V2V reconstruction.

In this work, only the data segments for $Re_\tau = 1148 \sim 1250$ were truncated from the whole DNS field. The average boundary thickness, determined by the height with 99 % of the free stream velocity, is approximately 1200 wall units, i.e. $\delta^+ \approx 1200$. The selection for this boundary thickness was based on two considerations. From the perspective of the V2V reconstruction, the logarithmic layer of this data segment covers a wall-normal range of approximately 160 wall units (from 80 wall units to $0.2\delta^+$), corresponding to an acceptable number of computational nodes for the V2V reconstruction. On the other hand, investigations (Tanahashi *et al.* 2004; del Álamo *et al.* 2006; Herpin *et al.* 2013; Wang *et al.* 2019) have validated that the fine-scale vortices populated in TBL present universal behaviours, independent of the Reynolds number. The truncated DNS data segment has a streamwise dimension of $8\delta^+$, a spanwise dimension of $13.4\delta^+$, and a wall-normal range from the viscous sublayer to $0.3\delta^+$, corresponding to a Cartesian grid of $1412 \times 4096 \times 91$. The variation range of the viscous wall unit in the DNS data segments is ± 0.8 %, which is small enough to be viewed as a constant. Totally, twelve frames of DNS fields were downloaded, providing sufficient data for deriving the statistical quantities. To minimize the processing errors, all the calculations in the present work were based on the original DNS grid. The derivative computations were performed via a 5-node central differential scheme. More parameters about the DNS data segments employed in this work are collected in table 1.

Throughout this article, the coordinate origin is located on the wall, and x, y, z align with the streamwise, spanwise and wall-normal directions, respectively. The variable t indicates the time dimension. $\boldsymbol{u}$ denotes the fluctuating velocity vector, obtained by subtracting the mean streamwise velocity component from the original DNS vector field; u, v, w designate the streamwise, spanwise and wall-normal fluctuating velocity components, respectively. A superscript of '+' indicates that the quantity is normalized by the wall unit or the friction velocity. Only the fluctuating velocity field is considered in the following analysis.

2.2. *The vortex identification*

Various vortex identification criteria were developed to extract filamentary (tube-like) vortices from turbulence. Most of them are based on local velocity gradient tensor ($\nabla \boldsymbol{u}$),

Friction Reynolds-number range	Wall unit variation	Streamwise range	Spanwise range	Wall-normal range
$Re_\tau = 1148 \sim 1250$	$\pm 0.8\,\%$	$8\delta^+$	$13.4\delta^+$	4.99–359.3
Total number of nodes	Total number of frames	Streamwise spacing (Δx^+)	Spanwise spacing (Δy^+)	Wall-normal spacing (Δz^+)
$1412 \times 4096 \times 91$	12	6.80	3.93	1.01–6.26

Table 1. A collection of parameters for the DNS data employed in this work.

including the second invariant Q (Hunt, Wray & Moin 1988), the discriminant Δ (Chong, Perry & Cantwell 1990), the swirl strength λ_{ci} (Zhou *et al.* 1999), the λ_2 criterion (Jeong & Hussain 1995) and so on. Commonly, the iso-surfaces of the criterion for one prescribed value are displayed as recognized vortices. Chakraborty *et al.* (2005) revealed the relationships between these identification criteria and demonstrated that results from different criteria are approximately equivalent for turbulent flows. Among these criteria, the swirl strength (λ_{ci}) corresponds to the imaginary part of the complex eigenvalue of the velocity gradient tensor, which has the same dimension as vorticity. A lot of investigators (Ganapathisubramani *et al.* 2006; Hambleton, Hutchins & Marusic 2006; Lee & Sung 2009) used 'signed swirl' as the representative variable for the in-plane component of a vortex, which is obtained by multiplying λ_{ci} by the sign of the out-of-plane component of vorticity. For eduction purposes, Pirozzoli *et al.* (2010) defined the strength of vortex tubes by introducing a 'vorticity-like' variable, which is equal to $2\lambda_{ci}$.

As for the vortex orientation, Gao *et al.* (2011) and Tian *et al.* (2018) suggested using the real eigenvector of ∇u (denoted as Λ_r). Tian *et al.* (2018) gave a mathematical discussion on the definition of the vortex vector based on the Schur decomposition theory (Gentle 1998). According to the viewpoint of Tian *et al.* (2018), the vortex orientation (Λ_r) corresponds to a direction with zero rotation speed. As indicated by the definition of velocity gradient tensor (∇u), the relative velocity δu for two points separated by a small position vector δr could be expressed as

$$\delta u = \nabla u \cdot \delta r. \tag{2.1}$$

The non-rotation requirement means that the relative velocity should be along δr, which means

$$\nabla u \cdot \delta r = \mu \delta r, \tag{2.2}$$

where μ should be a real constant. The above equation implies that δr is the real eigenvector of ∇u, viz. Λ_r.

Considering the eigenvector (Λ_r) contains no sign information about rotation, the local vorticity ω is used as a reference. Specifically, the eigendirection (Λ_r or $-\Lambda_r$) forming an acute included angle with ω is viewed as the vortex orientation. In this work, for the convenience of numerical implementation, the swirl strength λ_{ci} and the orientation vector Λ_r are combined to define a vector field as

$$\Lambda = \lambda_{ci}\text{sign}(\Lambda_r \cdot \omega)\Lambda_r, \tag{2.3}$$

where 'sign' is the sign function, returning the sign of the bracketed variable. Throughout this article, the vortex field refers to Λ as default, which is consistent with the definition by

Wang *et al.* (2019). It should be remembered that (2.3) is not a widely accepted expression since no mathematical definition for a vortex is available so far. In this work, the vortex field serves as a carrier for the geometrical and strength information of tubular vortices, which is necessary for the V2V reconstruction. In the following § 3, we will inspect the definition of (2.3) from the respect of the geometrical property of the recognized vortices.

2.3. *The correlation coefficient and the complex coherence spectrum*

A successful V2V reconstruction should return a velocity field sharing a high degree of similarity with the original DNS field, which can be measured by the correlation coefficient (*CC*). The *CC* is an indicator of the linear correlation degree between two input signals. In the current investigation, the *CC* for the reconstructed/original streamwise velocity components at one wall-normal position (z_0) is calculated by

$$CC(z_0) = \frac{\langle u_{rec}(x, y, z_0, t) u_{DNS}(x, y, z_0, t) \rangle_{x,y,t}}{\sqrt{\langle u_{rec}(x, y, z_0, t)^2 \rangle_{x,y,t} \langle u_{DNS}(x, y, z_0, t)^2 \rangle_{x,y,t}}}. \tag{2.4}$$

Herein, $u_{rec}(x, y, z, t)$ and $u_{DNS}(x, y, z, t)$ denote the reconstructed streamwise velocity component field and the corresponding DNS field; $\langle \cdot \rangle_{x,y,t}$ represents the ensemble average, which is implemented by averaging the quantities in the brackets along the homogeneous dimensions, including the temporal dimension (t) and the wall-parallel dimensions (x and y), as indicated by the subscript x, y, t. The *CC*s regarding other velocity components (v and w) are calculated based on similar expressions with (2.4).

As a refined variant for *CC*, the complex coherence spectrum (*CCS*) measures the scale-specific linear coherence of two input signals (Stoica & Moses 2005; Ramirez, Via & Santamaria 2008). In the current work, the *CCS* formula takes a form resembling the correlation coefficient, but in the spectral representation. Specifically, the streamwise *CCS* between $u_{rec}(x, y, z, t)$ and $u_{DNS}(x, y, z, t)$ at a given wall-normal position (z_0) could be calculated by

$$CCS(k) = \frac{\langle \tilde{u}_{rec}(k, y, z_0, t) \tilde{u}_{DNS}(k, y, z_0, t)^* \rangle_{y,t}}{\sqrt{\langle \tilde{u}_{rec}(k, y, z_0, t) \tilde{u}_{rec}(k, y, z_0, t)^* \rangle_{y,t} \langle \tilde{u}_{DNS}(k, y, z_0, t) \tilde{u}_{DNS}(k, y, z_0, t)^* \rangle_{y,t}}}. \tag{2.5}$$

In (2.5), $\tilde{u}_{rec}(k, y, z_0, t)$ and $\tilde{u}_{DNS}(k, y, z_0, t)$ denotes the streamwise (1-D) Fourier-transform coefficient of $u_{rec}(x, y, z, t)$ and $u_{DNS}(x, y, z, t)$, respectively; k denotes the corresponding wavenumber. For convenience, $\tilde{u}_{rec}(k, y, z_0, t)$ and $\tilde{u}_{DNS}(k, y, z_0, t)$ are simply represented by $\tilde{u}_{rec}(k)$ and $\tilde{u}_{DNS}(k)$ in the following discussions. Notably, both $\tilde{u}_{rec}(k)$ and $\tilde{u}_{DNS}(k)$ are complex numbers, carrying the scale-specific amplitude and phase information of the input velocity fields. The asterisk designates the complex conjugate operation; $\langle \cdot \rangle_{y,t}$ indicates averaging the quantities in the brackets along the temporal dimension and the spanwise direction, which is simply denoted as $\langle \cdot \rangle$ in the following discussions. Equation (2.5) results in a complex number, which is different from the linear coherence spectrum (*LCS*) used by Baars & Marusic (2020*a*). In their work, the *LCS* was defined as the squared magnitude of the current *CCS*, which measures the scale-by-scale coupling degree for two-point velocity signals. The phase angle of the *CCS* indicates the scale-by-scale phase deviation, which is also considered as the indicator for accessing the V2V reconstruction.

To illuminate the physical implication of (2.5), we express $\tilde{u}_{rec}(k)$ and $\tilde{u}_{DNS}(k)$ by the exponential forms, viz. $\tilde{u}_{rec}(k) = A_{rec}(k) \, e^{i\gamma_{rec}(k)}$ and $\tilde{u}_{DNS}(k) = A_{DNS}(k) \, e^{i\gamma_{DNS}(k)}$.
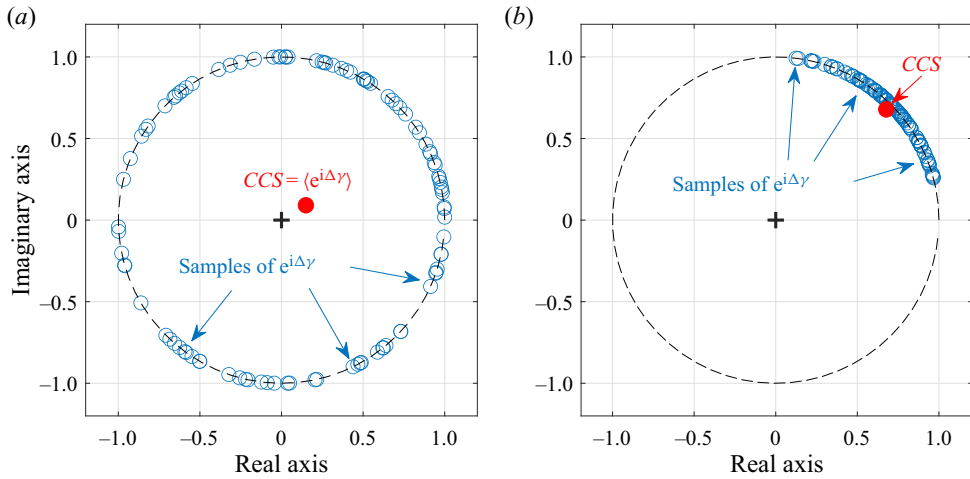
Figure 1. Schematic plots for illustrating the relation between *CCS* and the distribution of the phase deviations ($\Delta\gamma$) for a set of input signal samples. The sample data of $e^{i\Delta\gamma}$ are schematically displayed in the complex coordinate system by hollow blue circles. The red dot, which is the centre of the blue circles, marks the position of *CCS* ($CCS(k) = \langle e^{i\Delta\gamma}\rangle$). Panel (*a*) corresponds to the situation with a small *CCS* magnitude; (*b*) corresponds to the situation with a large *CCS* magnitude.

Herein, $A_{rec}(k)$ and $A_{DNS}(k)$ stand for the amplitudes of $\tilde{u}_{rec}(k)$ and $\tilde{u}_{DNS}(k)$, respectively; $\gamma_{rec}(k)$ and $\gamma_{DNS}(k)$ indicate the corresponding phase angles. By substituting $\tilde{u}_{rec}(k)$ and $\tilde{u}_{DNS}(k)$ in (2.5) with their exponential forms, it could be easily derived that

$$CCS(k) = \langle \hat{A}_{rec}(k)\hat{A}_{DNS}(k)\, e^{i\Delta\gamma(k)}\rangle. \tag{2.6}$$

In (2.6), $\hat{A}_{rec}(k) = A_{rec}(k)/\sqrt{\langle A_{rec}(k)^2\rangle}$ and $\hat{A}_{DNS}(k) = A_{DNS}(k)/\sqrt{\langle A_{DNS}(k)^2\rangle}$, which could be viewed as the normalized amplitudes; $\Delta\gamma(k) = \gamma_{rec}(k) - \gamma_{DNS}(k)$ represents the phase deviation between $\tilde{u}_{rec}(k)$ and $\tilde{u}_{DNS}(k)$; $e^{i\Delta\gamma(k)}$ is the polar representation for the phase deviation $\Delta\gamma(k)$. Equation (2.6) means that the *CCS* equals the weighted average of the sample data for $e^{i\Delta\gamma(k)}$, and the corresponding weighting coefficients are $\hat{A}_{rec}(k)\hat{A}_{DNS}(k)$.

For the sake of clarity, we first disregard the weighting coefficient and consider the special case of $LCS(k) = \langle e^{i\Delta\gamma(k)}\rangle$. In this case, the *CCS* is determined by the phase deviation between $\tilde{u}_{rec}(k)$ and $\tilde{u}_{DNS}(k)$. If $\tilde{u}_{rec}(k)$ and $\tilde{u}_{DNS}(k)$ are extremely incoherent in phase, their phase deviation, deemed as a random variable, would present a uniform probability distribution between 0 and 2π. In the complex coordinate system (as shown by figure 1*a*), the samples of $e^{i\Delta\gamma(k)}$ (blue circles) would be spread evenly on the unit circle around the origin. Thus, the centre of these scattered numbers (i.e. the statistical average, *CCS*) would occur very close to the origin. On the contrary, if the $\tilde{u}_{rec}(k)$ and $\tilde{u}_{DNS}(k)$ are coupled in phase, these hollow circles would cluster towards one specific orientation (as shown in figure 1*b*). The central point (the red dot) would be in close proximity to the unit circle, giving a *CCS* with a magnitude close to one. The above explanation can be extended to the general cases of (2.6), as long as these scattered sampling points are given different weighting coefficients when calculating the central point. In this sense, the *CCS* incorporates both the phase and magnitude information from $\tilde{u}_{rec}(k)$ and $\tilde{u}_{DNS}(k)$, and provides a comprehensive diagnosis on their scale-specific coherence relation.
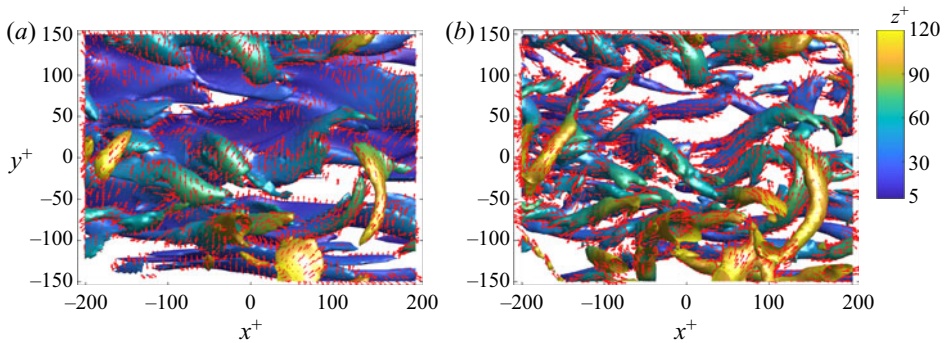
Figure 2. Instantaneous flow structures identified by vorticity magnitude (*a*) and vortex magnitude (*b*). The surfaces in the two plots correspond to $\omega^+ = 0.42$ and $\lambda_{ci}^+ = 0.10$ respectively, coloured based on the distance from the wall. Orientations of vorticity and vortex on the surfaces are also displayed by red vectors. For clarity, only one in four vectors in each direction are shown.

3. The geometrical property of the vortex field

As the cornerstone of the V2V reconstruction, the vortex field defined in § 2.2 merits a special discussion. This section will focus on the geometrical property of the vortex field. To start this discussion, an observation on the instantaneous field is beneficial. Figure 2 shows the structures identified by iso-surfaces of vorticity magnitude (ω) and vortex intensity (λ_{ci}), with orientation vectors displayed on the surfaces. For a clear display, only the iso-surfaces for $z^+ \leq 120$ are shown in the figure. Since both ω and λ_{ci} are calculated based on the fluctuating velocity field, the influence of mean shear in TBL has been removed. The thresholds for ω and λ_{ci} are prescribed so that the identified structures occupy approximately 10 % of the total volume displayed. Distinct characteristics for the ω-identified and λ_{ci}-identified structures are noticed. The former contains large bulks of flat sheet-like entities at the lower layer and thin tube-like entities above. The latter recognizes only the vortex tubes with a thickness of about ten wall units. In figure 2(*b*), several vortex tubes incline at an angle of approximately 45° with respect to the streamwise direction, which is similar to the criss-cross patterns observed by Bandyopadhyay (1989) in the laser-light-sheet smoke flow visualization pictures. While a typical hairpin vortex is not observed, there are some vortex tubes resembling twisted single-leg hairpin vortices. Mostly, the vortex vectors are attached in the vortex surface and pointing to the extending direction of the vortex tubes. This property has also been reported by Tian *et al.* (2018), who regarded it as a support for their definition of vortex orientation. For the vorticity field, the property does not hold at the near-wall region, where the vorticities tend to be aligned with the spanwise direction. A correlated work involving this property is reported by Xiong & Yang (2019), who attempted to calculate the 'vorticity surface field' based on the vorticity field. A scalar field is called the vorticity surface field if the normal vector of its iso-surface is perpendicular to the local vorticity vector. If this concept is used for the present vortex field, we can see that λ_{ci} could be approximately regarded as the 'vortex surface field'.

To quantitatively analyse the relationship between the vortex surface and the vortex orientation, we resort to the differential geometry, which is a useful mathematical tool to describe the local curvatures of a surface. Consider a small vortex surface element S as shown in figure 3(*a*), which can be viewed as a quadratic surface; $\mathbf{n}$ denotes the normal vector of S, pointing to the side with smaller vortex magnitude. Generally, two orthogonal principal directions (indicated by two unite vectors: $\boldsymbol{\kappa}_1$ and $\boldsymbol{\kappa}_2$) can be determined on
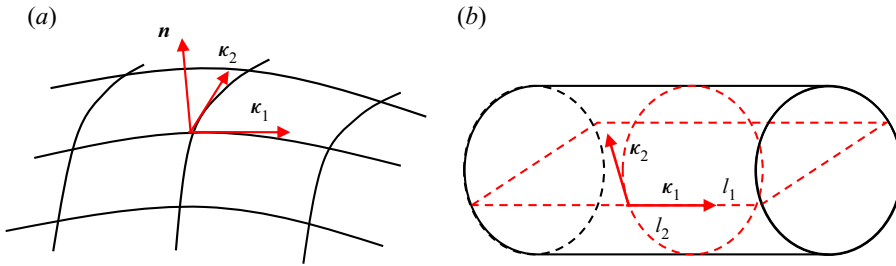
(a)   (b)

Figure 3. Diagrammatic sketches for the principal directions of the local curvatures.

S, which correspond to the directions with the maximum and minimum curvatures, respectively; κ_1 and κ_2 refer to the first principal direction and the second principal direction for the local curvatures. Taking an example of a straight vortex tube with a uniform radius (see figure 3b), the two principal directions (κ_1 and κ_2) are aligned with the axial direction and azimuthal direction, respectively. The corresponding curvatures for κ_1 and κ_2 refer to the local curvatures of lines extracted along the two directions from the surface (see l_1 and l_2 in figure 3b), which are 0 and $-1/R$ respectively. The negative sign indicates that the extracted line (l_2) bends toward the negative direction of $\boldsymbol{n}$. Thus, we can see that the vortex orientation is aligned with κ_1 for a straight vortex tube. For general thin and tube-like vortices, one can guess that the vortex orientation also tends to align with κ_1, which will be tested and verified in the following discussion.

For each point in the vortex field, the vortex surface passing this point could be extracted, and correspondingly the normal vector $\boldsymbol{n}$ and the principal directions (κ_1 and κ_2) can be determined. Detailed introduction for this process is provided in Appendix A of this article; κ_1, κ_2 and $\boldsymbol{n}$ constitute a local coordinate system, and we can investigate the vortex orientation in this local coordinate system. Specifically, a transformation from the global coordinate system to this local coordinate system is performed on the vortex vector. Subsequently, in the local coordinate system, the vortex vector is further expressed by three spherical coordinates: radical distance (ρ), azimuth angle (ψ) and zenith angle (θ). The joint p.d.f. of ψ and θ is calculated based on the data points with $\lambda_{ci}^+ > 0.10$ and $z^+ \leq 0.3\delta^+$. The threshold, which is consistent with the one used in figure 2, is deployed here to exclude the influence of weak vortices. The resulting p.d.f. is further normalized by $\sin(\theta)$ before displayed on a unit sphere surface (figure 4) in order to reflect the local areal density of probability, which is called a spherical p.d.f..

In figure 4, only a quarter of a complete sphere is contoured since κ_1, κ_2 could change direction by 180°, blurring the definitions of vortex orientation in these four quarters. As a reference, the spherical p.d.f. for vorticity orientation in the curvature coordinates of the vorticity magnitude is also provided. As we can see, two concentrations of the spherical p.d.f. for the vorticity orientation are observed nearby the axes of κ_1 and κ_2 (figure 4a). Differently, the spherical p.d.f. for vortex orientation shown in figure 4(b) presents an extremely dense distribution along the κ_1 direction. Specifically, the largest probability density appearing nearby κ_2 axis is approximately 6.8, which is 21 times as large as the average probability on the sphere quarter ($1/\pi$). This verifies that the vortex vector has a strong disposition to be aligned with the first principal direction of vortex surface curvature. What is noteworthy is that the first principal direction for curvature also corresponds to the direction along which the vortex magnitude changes the least. Thus, we can restate that the vortex orientation tends to be aligned with the slowest-changing direction of the vortex magnitude. The above discussion reveals an interesting aspect of the relationship between the vortex orientation and the vortex magnitude. It indicates that
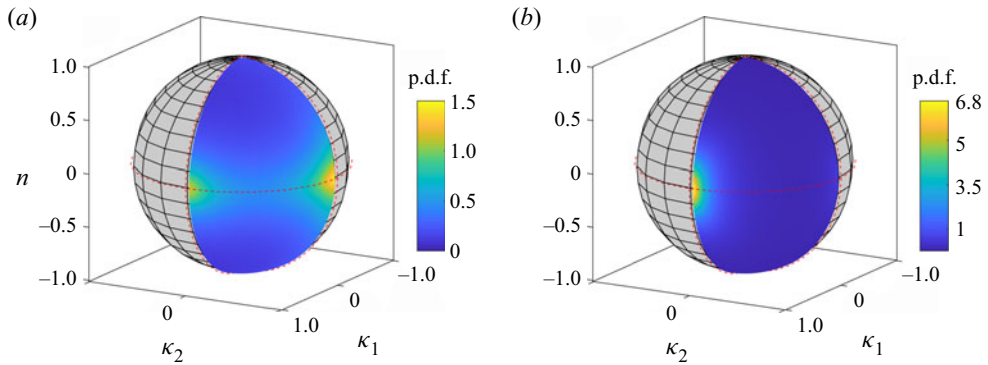
Figure 4. The spherical p.d.f. for $\boldsymbol{\omega}$ (*a*) and $\boldsymbol{\Lambda}$ (*b*) orientations in the coordinate system of the local curvatures. Note that the colour scales in the two panels are different for better visualization.

the swirl strength λ_{ci} and the eigenvector $\boldsymbol{\Lambda}_r$ are closely associated and thus combining them to define a vortex vector as we did in this work makes some sense. Finally, it should be pointed out that the alignment property holds for comparatively smooth vortex tubes. For the complex vortices such as a bursting vortex (Bandyopadhyay 2020), the alignment trend is more likely to be obscured.

Based on the above geometrical property, the tube-like vortices could be simplified as 3-D curved centrelines along with a Gaussian distribution of vortex intensity in the cross-sections, which would lead to a significant reduction in the description variables. Lundgren (1982) validated that the spiral vorticity distribution in the cross-section is necessary in producing the $-5/3$ law of the energy spectra for isotropic turbulence. Thus, simple line-vortex elements with an axisymmetric intensity distribution may not be complete in describing the turbulent motions in the inertial range. In addition, reducing vortices to line elements requires sophisticated processing steps, which might introduce artificial or unphysical factors into the final results. Therefore, in the present investigation, we directly employ the vortex fields as the input information for the V2V reconstruction.

Before shifting to the subject of the V2V reconstruction, a further discussion on the use of vorticity and vortex in turbulence representation and modelling is beneficial. In earlier investigations, each one of the blob-like, sheet-like and tube-like vorticity models was used as the constructing elements for isotropic turbulence (Synge & Lin 1943; Townsend 1951; Corrsin 1962; Tennekes 1968). Kuo & Corrsin (1972) provided convincing evidence that the fine-scale turbulence was more likely to be the collections of vortex tubes than other possibilities. Vortex tubes are preferred because sheet-like structures have a strong tendency to roll up (Lundgren 1982). In the wall-turbulence community, the hairpin vortex model or attached eddy model could also be represented by a combination of vortex tubes. Also, large numbers of research works (Tanahashi *et al.* 2004; del Álamo *et al.* 2006; Stanislas *et al.* 2008; Wang *et al.* 2019) have revealed the universal behaviours of tubular vortices in the radius, intensity, orientation and correlation functions. The discussion provides more evidence that the tube-like vortices should be viewed as the building blocks, supporting the following efforts to reconstruct wall turbulence based on them.

4. The V2V reconstruction

The primary challenge for the V2V reconstruction is the information loss caused by the vortex identification process. To fill the information gap, empirical parameters or

data-driven models should be introduced in the V2V reconstruction. On the other hand, a linear reconstruction scheme is preferred because it benefits both physical interpretation and numerical implementation. The linear reconstruction scheme is based on the opinion that the induced velocity field by a vortex field could be regarded as the superposition of the inducing effects from individual vortices, which is familiar in the attached eddy model (Townsend 1956).

Based on these considerations, we resort to the linear stochastic estimation (LSE) for the V2V reconstruction. Generally, LSE attempts to estimate the unknown variables based on the known variables by a linear expression containing empirical parameters. In the wall-bounded turbulence community, the application of LSE in extracting conditionally averaged structures has been widely reported; see Adrian (1994), Christensen & Adrian (2001), and Wang *et al.* (2019). In these works, LSE served to estimate the neighbouring velocities of a reference even occurring at one spatial position, which is basically a point-based (zero dimension) estimation. As an extension, LSE based on 1-D signals has been reported by Tinney *et al.* (2006), who developed the so-called spectral LSE for this purpose. When it comes to the V2V reconstruction, the problem is to estimate one 3-D field (velocity field) based on another 3-D field (vortex field), which is a 3-D-to-3-D estimation and has not been reported in the wall-turbulence community. In this section, the V2V reconstruction problem will be discussed under the general theoretical framework of LSE and the general governing equations will be deduced. Subsequently, the V2V reconstruction regarding wall-bounded turbulence is focused on, and the homogeneous condition in the wall-parallel plane is employed to simplify the governing equations. Finally, the corresponding implementation scheme and several considerations will be introduced in detail.

For the convenience of the following discussion, we give the conventions for symbols first. Let u and Λ with a subscript i or j denote the ith or the jth component of velocity and vortex ($i = 1, 2, 3$; $j = 1, 2, 3$). Einstein's summation convention is adopted so that two repeated indices occurring in one term automatically trigger a summation for all possible realizations of these indices; $\boldsymbol{r} = (x, y, z)$, $\boldsymbol{r'} = (x', y', z')$ denote 3-D spatial position vectors in the considered spatial domain (denoted as Ω).

4.1. *The general theory for the V2V reconstruction*

Denote $\hat{u}_i$ as the estimation variable for u_i, and suppose that $\hat{u}_i$ could be expressed by linear operators ($\mathcal{L}_{ij}$) acting on Λ_j, which yields

$$\hat{u}_i = \mathcal{L}_{ij}\Lambda_j, \tag{4.1}$$

where $[\mathcal{L}_{ij}]$ is a 3×3 matrix of linear operators. The linear operators can be viewed as continuous transformations on Λ_j, and no limitations on their realization forms are needed in this general analysis. (4.1) is a general form for the V2V reconstruction, and $\mathcal{L}_{ij}$ needs to be determined by minimizing the reconstruction deviations.

Considering both $\hat{u}_i$ and u_i are 3-D vector fields, their deviation (D) can be defined by an integral form as

$$D = \iiint_{\Omega} (\hat{u}_i - u_i)(\hat{u}_i - u_i)\, \mathrm{d}\Omega \Big/ \iiint_{\Omega} \mathrm{d}\Omega. \tag{4.2}$$

Facilitated by the above definition, the optimal $\mathcal{L}_{ij}$ can be determined by minimizing the deviation in a statistical sense, i.e.

$$\min\langle D\rangle, \tag{4.3}$$

where $\langle \cdot \rangle$ represents an ensemble average.

According to the calculus of variation (Appendix B), the above optimization problem is equivalent to the following equations,

$$\mathcal{L}_{ij}\langle \Lambda_j \Lambda_m(\boldsymbol{r}')\rangle = \langle u_i \Lambda_m(\boldsymbol{r}')\rangle \quad for \; \forall \, \Lambda_m(\boldsymbol{r}') \; (\boldsymbol{r}' \in \Omega; m = 1, 2, 3). \tag{4.4}$$

Equations (4.4) constitute the governing equations for the linear operators $\mathcal{L}_{ij}$. Note that both Λ_j and u_i are 3-D functions of the implicit position vector $\boldsymbol{r}$, and $\langle \Lambda_j \Lambda_m(\boldsymbol{r}')\rangle$ should also be regarded as a 3-D function of $\boldsymbol{r}$ rather than $\boldsymbol{r}'$ when the linear operators ($\mathcal{L}_{ij}$) act on it. For any given $\Lambda_m(\boldsymbol{r}')$, the form of $\langle \Lambda_j \Lambda_m(\boldsymbol{r}')\rangle$ or $\langle u_i \Lambda_m(\boldsymbol{r}')\rangle$ indicates a conditional average for the event $\Lambda_m(\boldsymbol{r}')$. Here, $\langle \Lambda_j \Lambda_m(\boldsymbol{r}')\rangle$ can be understood as the averaged vortex distribution given an event of Λ_m occurring at $\boldsymbol{r}'$, and similarly, $\langle u_i \Lambda_m(\boldsymbol{r}')\rangle$ could be viewed as the conditionally averaged velocity distribution. The operators $\mathcal{L}_{ij}$ always act on the local statistical vortex distribution and return the corresponding velocity distribution.

Equation (4.4) are comparable to the Yule–Walker equation from classical LSE (Adrian 1994). The latter was established to determine the unknown parameters in the estimating expression, the number of which is usually small or finite at least. In this work, (4.4) is established to determine the linear operators $\mathcal{L}_{ij}$, which have infinite dimensions. The starting point of the current method is to estimate one 3-D field based on another given 3-D field, which is named field-based linear stochastic estimation (FLSE) in this work.

For a general case, the discretizing of (4.4) leads to a linear system with huge numbers of variables. For examples, if the spatial domain is discretized into $N_x \times N_y \times N_z$ computation nodes, numbers of the undetermined variables in $\mathcal{L}_{ij}$ would be $(3 \times N_x \times N_y \times N_z)^2$, which might be huge for a typical case. Fortunately, for wall-bounded turbulence flows such as the turbulent channel flow and TBL, the flow can be regarded as homogeneous in the wall planes, at least for a limited streamwise range. The homogeneous property would significantly reduce the numbers of variables and will be discussed in the following subsection.

For the convenience of the following discussion, denote that

$$R_{jm}(\boldsymbol{r}, \boldsymbol{r}') = \langle \Lambda_j \Lambda_m(\boldsymbol{r}')\rangle, \tag{4.5}$$

$$q_{im}(\boldsymbol{r}, \boldsymbol{r}') = \langle u_i \Lambda_m(\boldsymbol{r}')\rangle. \tag{4.6}$$

Thus (4.4) can be rewritten as

$$\mathcal{L}_{ij} R_{jm}(\boldsymbol{r}, \boldsymbol{r}') = q_{im}(\boldsymbol{r}, \boldsymbol{r}') \quad for \; \forall \, \boldsymbol{r}' \in \Omega; m = 1, 2, 3. \tag{4.7}$$

4.2. *FLSE for wall-bounded turbulence*

The estimated velocity $\hat{u}_i$ could be viewed as a result of the joint inducing effects caused by the neighbouring vortices. Suppose that the inducing effect of a vortex field could be expressed as an integral of the inducing effects of vortex vectors at different locations, which yields a form of integral transformation as

$$\hat{u}_i(\boldsymbol{r}) = \iiint_{\Omega} \varphi_{ij}(\boldsymbol{r}; \boldsymbol{r}') \Lambda_j(\boldsymbol{r}') \, \mathrm{d}x' \, \mathrm{d}y' \, \mathrm{d}z'. \tag{4.8}$$

In the equation, $\varphi_{ij}(\boldsymbol{r}; \boldsymbol{r}')$ is a kernel function, which indicates the contribution of $\Lambda_j(\boldsymbol{r}')$ with unit magnitude to the ith velocity component at the position $\boldsymbol{r}$. Equation (4.8) provides a specific realization form for the linear operator $\mathcal{L}_{ij}$.

For wall-bounded turbulence, as discussed before, the flow could be treated as a homogeneous field in the x–y plane. Thus, the inducing effect of a vortex should keep

922 A18-14

invariable when its position is shifted in the x–y plane, which yields

$$\varphi_{ij}(\boldsymbol{r}; \boldsymbol{r}') = \varphi_{ij}(x, y, z; x', y', z') = \varphi_{ij}(x - x', y - y', z; 0, 0, z'). \quad (4.9)$$

For simplicity, it is denoted that

$$\varphi_{ij}(x - x', y - y', z; 0, 0, z') = \varphi_{ij}(x - x', y - y', z; z'). \quad (4.10)$$

By the way, such a shifting-invariable property also holds for $R_{jm}(\boldsymbol{r}, \boldsymbol{r}')$ and $q_{im}(\boldsymbol{r}, \boldsymbol{r}')$, thus we also have $R_{jm}(x, y, z; z')$ and $q_{im}(x, y, z; z')$ as the simplifications for $R_{jm}(x, y, z; 0, 0, z')$ and $q_{im}(x, y, z; 0, 0, z')$.

Combining (4.8) and (4.9), we have

$$\hat{u}_i(\boldsymbol{r}) = \iiint_{\Omega} \varphi_{ij}(x - x', y - y', z; z') \Lambda_j(\boldsymbol{r}') \, \mathrm{d}x' \, \mathrm{d}y' \, \mathrm{d}z',$$
$$= \int_{z'} \left(\iint_{x'-y'} \varphi_{ij}(x - x', y - y', z; z') \Lambda_j(\boldsymbol{r}') \, \mathrm{d}x' \, \mathrm{d}y' \right) \mathrm{d}z'. \quad (4.11)$$

The bracketed term is a 2-D convolution operation in the x–y plane, which could be denoted as an asterisk. Thus, (4.11) can be simplified as

$$\hat{u}_i(\boldsymbol{r}) = \mathcal{L}_{ij} \Lambda_j = \int_{z'} \varphi_{ij}(\cdot, \cdot, z; z') * \Lambda_j(\cdot, \cdot, z') \, \mathrm{d}z', \quad (4.12)$$

where the position variables x and y are substituted as dots, indicating the convolution works in the x–y plane. Equation (4.12) is the formula for the so-called V2V reconstruction, where $\varphi_{ij}(x, y, z; z')$ needs to be determined first. By definition, $\varphi_{ij}(x, y, z; z')$ reflects the inducing effect of an individual vortex vector at different wall-normal positions, which is named the inducing model function in this work.

Substituting the linear operators in (4.7) by the explicit expression of (4.12), the governing equations for $\varphi_{ij}(x, y, z; z')$ are obtained as

$$\int_{z''} \varphi_{ij}(\cdot, \cdot, z; z'') * R_{jm}(\cdot, \cdot, z''; z') \, \mathrm{d}z'' = q_{im}(x, y, z; z') \quad \text{for } \forall z'; m = 1, 2, 3. \quad (4.13)$$

Note that only the equations for $x' = 0$ and $y' = 0$ in (4.7) are collected into (4.13) since the number for unknown variables have been significantly reduced by using the homogeneous condition.

4.3. *Discretization and implementation for FLSE*

Equations (4.13) need to be solved in the discrete form. Suppose that the domain is discretized as $N_x \times N_y \times N_z$ computation nodes, and we use the symbols a, b, c, c', c'' as the indices for discretized variables of x, y, z, z', z'', respectively. The integral operation could be discretized as a summation implied by the repeated subscript of c''. Thus, we have

$$\varphi_{ij}(\cdot, \cdot, z_c; z''_{c''}) * R_{jm}(\cdot, \cdot, z''_{c''}; z'_{c'}) = q_{im}(x_a, y_b, z_c; z'_{c'}) \quad \text{for } \forall c', m. \quad (4.14)$$

Equation (4.14) is a linear system with underdetermined variables of $\varphi_{ij}(x_a, y_b, z_c; z''_{c''})$ for all the realizations of i, j, a, b, c, c''. The asterisk herein indicates the discrete convolution operation. Consistent with the former regulation, x_a, y_b are omitted in (4.14) in order to indicate the working dimensions for the convolution operation. The regulation also avoids

the occurrence of repeated a, b, which would cause confusion by erroneously triggering the automatic summation.

The number of underdetermined variables corresponding to all the possible realizations of i, j, a, b, c, c'' is $3 \times 3 \times N_x \times N_y \times N_z \times N_z$, which might be of the order of 10^9. Fortunately, these variables do not need to be solved simultaneously. Closer observation on the indices occurring in the left term of (4.14) reveals that the indices i and c occur only once, which implies that $\varphi_{ij}(x_a, y_b, z_c; z''_{c''})$ could be independently solved for the two indices. Specifically, for any prescribed indices i and c, the equations from (4.14) constitute a closed linear system with respect to all the realizations of $\varphi_{ij}(x_a, y_b, z_c; z''_{c''})$ for $\forall j, a, b, c''$, which could be written as a matrix form.

$$\boldsymbol{R}\boldsymbol{\varphi}^{i,c} = \boldsymbol{q}^{i,c}, \tag{4.15}$$

where $\boldsymbol{R}$ is a matrix formed by arranging the realizations of $R_{jm}(x_a, y_b, z''_{c''}; z'_{c'})$; $\boldsymbol{\varphi}^{i,c}, \boldsymbol{q}^{i,c}$ are vectors formed by collecting all the realizations of $\varphi_{ij}(x_a, y_b, z_c; z''_{c''})$ and $q_{im}(x_a, y_b, z_c; z'_{c'})$ for prescribed indices i and c. In this way, equations (4.14) could be divided into $N_z \times 3$ sets of reduced equations based on the different combinations of indices i and c. Each set of equations contains $3 \times N_x \times N_y \times N_z$ variables and can be solved independently.

Besides directly solving (4.15), the problem could also be efficiently solved by using fast Fourier-transform (FFT) technique. We perform 2-D discrete FFT in the x–y plane on each term of (4.14), and apply the well-known convolution theorem of FFT. Let $\tilde{R}_{jm}, \tilde{\varphi}_{ij}$ denote the FFT results of R_{jm}, φ_{ij}, and k_α, k_β indicate the discrete wavenumbers along the x, y direction. Thus we have

$$\sum_{c'', j} \tilde{R}_{jm}(k_\alpha, k_\beta, z''_{c''}; z'_{c'}) \tilde{\varphi}_{ij}(k_\alpha, k_\beta, z_c; z''_{c''}) = \tilde{q}_{im}(k_\alpha, k_\beta, z_c; z'_{c'}) \quad \text{for } \forall c', m. \tag{4.16}$$

Einstein's summation convention is abandoned in this equation since the repeated indices α, β do not imply a summation here. For numerical implementation, (4.16) should also be written as the matrix form. In this case, we can see $\tilde{\varphi}_{ij}(k_\alpha, k_\beta, z_c; z''_{c''})$ is independent with the indices of i, α, β, c. Therefore, for fixed indices of i, α, β, c, we can collect all realizations for $\tilde{R}_{jm}(k_\alpha, k_\beta, z''_{c''}; z'_{c'})$ and arrange them into a matrix ($\boldsymbol{A}^{\alpha,\beta}$). Similarly, $\tilde{\varphi}_{ij}$ and $\tilde{q}_{im}$ are arranged as vector forms as $\boldsymbol{\varphi}^{i,\alpha,\beta,c}$ and $\boldsymbol{b}^{i,\alpha,\beta,c}$ for prescribed indices i, α, β, c.

Facilitated by these conventions, (4.16) could be rewritten as

$$\boldsymbol{A}^{\alpha,\beta}\boldsymbol{\varphi}^{i,\alpha,\beta,c} = \boldsymbol{b}^{i,\alpha,\beta,c}. \tag{4.17}$$

Einstein's summation convention is abandoned in this expression. For each set of indices i, α, β, c, the equations of (4.17) constitute a closed linear system for $\boldsymbol{\varphi}^{i,\alpha,\beta,c}$, which contains $N_z \times 3$ variables. After all the equations are solved, $\tilde{\varphi}_{ij}(k_\alpha, k_\beta, z_c; z''_{c''})$ is recovered based on all the results. Inverse FFT operation is subsequently performed on $\tilde{\varphi}_{ij}(k_\alpha, k_\beta, z_c; z''_{c''})$ to return $\varphi_{ij}(x_a, y_b, z_c; z''_{c''})$. For clarify, a procedure card illustrating the FFT implementation has been provided in Appendix C. This card also incorporates the strategy of dealing with the numerical instability issue, which will be introduced in the next subsection.

4.4. *Issues and considerations for numerical implementation*

Although the FFT implementation significantly improves the computation efficiency, some considerations need to be addressed. In theory, the convolution theorem for FFT exactly

holds for the circular convolution operation, which imposes a periodic extension on the input functions. If the computation domain Ω is not large enough, the magnitudes of R_{jm} or q_{im} would not decay sufficiently at borders. The periodic extension leads to strong disconnections on borders, which would cause numerical instability in the FFT results. Therefore, the windowed FFT technique is suggested to deal with this issue. In this situation, the FFT method would be viewed as an approximate method, whose accuracy depends on the computation domain and needs to be further validated by the results.

The numerical stability for solving (4.15) or (4.17) requires that $\boldsymbol{R}$ and $\boldsymbol{A}^{\alpha,\beta}$ should be sufficiently positive definite, which means all the eigenvalues should be larger than a positive critical number. In practical implementation, both $\boldsymbol{R}$ and $\boldsymbol{A}^{\alpha,\beta}$ have zeros or very small eigenvalues, which cause ill-posed systems. In order to avoid this problem, Tikhonov regularization (Kress 2014) is suggested to improve the numerical stability. Specifically, (4.15) and (4.17) are reshaped into the following forms

$$(\boldsymbol{R} + s\boldsymbol{I})\boldsymbol{\varphi}^{i,c} = \boldsymbol{q}^{i,c}, \tag{4.18}$$

$$(\boldsymbol{A}^{\alpha,\beta} + s\tilde{\delta}(k_\alpha, k_\beta)\boldsymbol{I})\boldsymbol{\varphi}^{i,\alpha,\beta,c} = \boldsymbol{b}^{i,\alpha,\beta,c}, \tag{4.19}$$

where $\boldsymbol{I}$ is the identity matrix and s is the regularization parameter. Einstein's summation convention is cancelled in the equation. Here, $\tilde{\delta}(k_\alpha, k_\beta)$ is the 2-D FFT result for a discrete 2-D Dirac function $\delta(x_a, y_b)$, which is defined as

$$\delta(x_a, y_b) = \begin{cases} 1 & \text{for } x_a = 0, \ y_b = 0 \\ 0 & \text{otherwise} \end{cases}. \tag{4.20}$$

In (4.18) and (4.19), s plays a role in improving the statistical convergence and controlling the smoothness of the solution, which will be tested in § 5.

The FFT implementation of FLSE is a reminiscence of spectral linear stochastic estimation (SLSE) proposed by Tinney *et al.* (2006). Baars, Hutchins & Marusic (2016) applied SLSE to predict the velocity signals in wall-bounded turbulence and refined the inner–outer interaction model proposed by Marusic, Mathis & Hutchins (2010). More recently, Baars & Marusic (2020*a*) developed a data-driven decomposition scheme to decouple inner–outer coherence based on SLSE. Basically, SLSE reconstructs the prediction for 1-D signal by minimizing the estimation error in spectral space, which avoids the phase mismatch issue. While expanding SLSE from one dimension to two dimensions in *x*-*y* plane is straightforward, further expanding to 3-D application needs special treatment for the wall-normal dimension. In this work, FLSE offers a general routine to estimate one field based on another, regardless of the dimensions. As the implementation of FLSE, the FFT method expands spectra-based LSE to 3-D application in wall-bounded turbulence.

5. Numerical validation and application of FLSE

This section will focus on the validation and application of FLSE. The correlation functions involved in the governing equations (4.13) and the solved inducing model functions will be displayed, which helps to illustrate how FLSE works, and also benefits the discussion about how to set the calculation domain and the regularization parameters. Subsequently, the performance of FLSE will be comprehensively compared with the Biot–Savart law with the aim of promoting the FLSE method. The performance of FLSE in recovering energy spectra will be accessed, which provides some reference for

vortex-based modelling works. A novel application of FLSE in shedding light on the energy contributions from different heights will be introduced, and the results will be linked to the topic of the inner–outer interaction. Furthermore, the high-order moments for FLSE-reconstructed fields will be evaluated, which will arouse discussions about the limitations of FLSE. At last, the V2V reconstructions based on threshold-filtered vortex fields will be investigated.

5.1. *The correlation functions: R_{jm} and q_{im}*

Before performing FLSE, the self-correlation function for vortex fields (R_{jm}) and vortex–velocity correlation function (q_{im}) need to be derived from the DNS data. In this work, these correlation functions are calculated based on twelve large-size instantaneous DNS fields (as shown in table 1). The ensemble average is implemented by averaging along the statistically uniform dimensions, including the *x–y* plane and the temporal dimension. Concretely, the two correlation functions are calculated by

$$R_{jm}(x, y, z; z') = \langle \Lambda_j(x_0 + x, y_0 + y, z)\Lambda_m(x_0, y_0, z')\rangle_{x_0, y_0, t}, \tag{5.1}$$

$$q_{im}(x, y, z; z') = \langle u_i(x_0 + x, y_0 + y, z)\Lambda_m(x_0, y_0, z')\rangle_{x_0, y_0, t}. \tag{5.2}$$

Noting that $\langle \cdot \rangle_{x_0, y_0, t}$ denotes averaging the bracketed quantity for all the realizations of x_0, y_0, t.

In order to avoid the resolution issue, the calculation is carried out on the original computational grid of DNS. The statistical range for correlation functions is set as $x^+ \in [-0.5\delta^+, 0.5\delta^+]$, $y^+ \in [-0.25\delta^+, 0.25\delta^+]$, $z^+ \in [5, 0.3\delta^+]$, resulting in a computation grid of $179 \times 155 \times 91$. The investigation of del Álamo *et al.* (2006) on the size of attaching clusters supported the aspect ratio prescribed in this work. The wall-normal range covers the whole buffer layer and logarithmic layer, which contains most of the vortex populations in TBL. It should be pointed out that the statistical range for correlation functions also determines the calculation domain of φ_{ij}, which is correlated with the reconstruction accuracy. More arguments for setting this statistical range will be emphasized in the following discussions.

Figure 5 displays contours of R_{11} and q_{11} as functions of *x* and *y* for three wall-normal positions ($z'^+ = z^+ = 15.4, 119.4, 359.3$). At first glance, these contours are reasonably smooth and symmetric, indicating that the statistical results are well converged. At $z^+ = 15.4$, streak patterns occur nearby the centre points for both R_{11} and q_{11}, which are imprints of the quasi-streamwise vortices and low-speed streaks populated in this region. When z^+ increase from 119.4 to 359.3, both R_{11} and q_{11} display a self-similar increase in size, supporting the famous attached eddy hypothesis. Distinctive characteristics for R_{11} and q_{11} are also observed: while R_{11} remains a sharp peak at the central point, q_{11} shows two flat peaks, filling a large portion of the area in the plots. At the edge of the wall-normal range considered ($z^+ = 359.3$), bulks of the two q_{11} peaks still remain in the calculation range although they appear to be truncated at the boundaries to some extent. A much larger statistical range is needed if one attempts to cover the whole pattern for q_{11} in the *x–y* plane at $z^+ = 359.3$, which poses a severe challenge for both the number of sampling DNS fields and the computing resources. The statistical range employed in this work is based on the comprehensive considerations on the computation efficiency we can bear and the reconstruction accuracy we have expected. In fact, most of the results in this work will focus on the regions below the logarithmic layer, particularly for $z^+ < 120$, where the correlation peaks for R_{11} is satisfyingly covered in the calculation range. More importantly, the resulting reconstruction accuracy in this region is good enough to promote
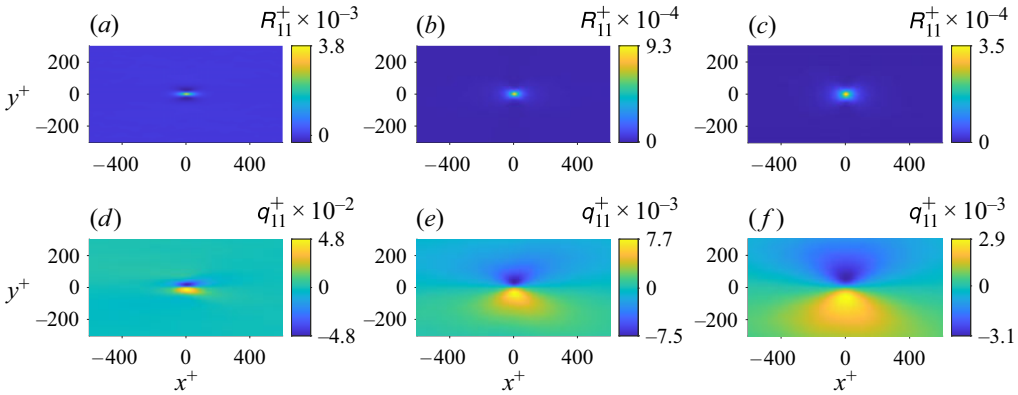
Figure 5. Contours of $R_{11}^+(x, y, z; z')$ (the first row) and $q_{11}^+(x, y, z; z')$ (the second row). From left to right, the contours correspond to $z^+ = z'^+ = 15.4$, $z^+ = z'^+ = 119.4$ and $z^+ = z'^+ = 359.3$, respectively.

the FLSE method and to draw some revealing conclusions as we can see in the following discussions.

Once R_{jm} and q_{im} for $i, j, m = 1, 2, 3$ are obtained, the vortex model function $\varphi_{ij}(x, y, z; z)$ can be solved based on (4.18) or (4.19). Considering the number of computation nodes involved is quite large (approximately 2.5 million) in this case, an FFT implementation scheme is employed based on the processing procedures shown in Appendix C. To avoid the interruptions at boundaries, both R_{11} and q_{11} are weighted by a Hanning window before the FFT operation. Weighting a signal by a Hanning window procedure will force the input signal to decay to zero at boundaries, which benefits the numerical stability. Testing on the Hanning window and the regularization parameter will be introduced in the following subsection.

5.2. *The regularization parameter and the Hanning window*

The performance of FLSE is determined by the inducing model functions. Figure 6 shows $\varphi_{13}(x, y, z; z)$ in the x–y plane, which reflects the in-plane inducing effect of the individual wall-normal vortex on the streamwise velocity component. Figure 6 displays the results from three calculation cases: two cases passing the typical processing routines with $s = 0.82 \times 10^{-6} \mu_{max}$ and $s = 0.82 \times 10^{-4} \mu_{max}$ respectively, and one case skipping Hanning window weighting before FFT with $s = 0.82 \times 10^{-4} \mu_{max}$. Herein, μ_{max} is the maximum eigenvalue for all the realizations of $\boldsymbol{A}^{\alpha,\beta}$. To make it clear, only a small region with a streamwise range of ± 150 and a spanwise range of ± 75 is displayed. It shows that while figures 6(*a,d*) and 6(*b,e*) show similar contours, the contour maps of figure 6(*c,f*) suffer from numerical issues and present spurious patterns. It indicates that the Hanning window is necessary for the FFT implementation of FLSE in order to obtain credible results. In figure 6(*a,d*) or figure 6(*b,e*), φ_{13} shows two streamwise-extending streaks at $z^+ = 15.4$, which reflects the basic flow feature in this region. At $z^+ = 119.4$, the streak patterns shrink along the streamwise direction and form a velocity distribution resembling an intense swirl in the x–y plane. The wall-normal variation of the inducing model function gives signs of adaption to local flow features, which is vital for the success of V2V reconstruction. By comparing figures 6(*a,d*) and 6(*b,e*), it can be found that adjusting the value of s works as a dilation or erosion effect on the φ_{13} pattern. Larger s helps to obtain smoother and more symmetrical contour patterns, which implies a good convergence. For a
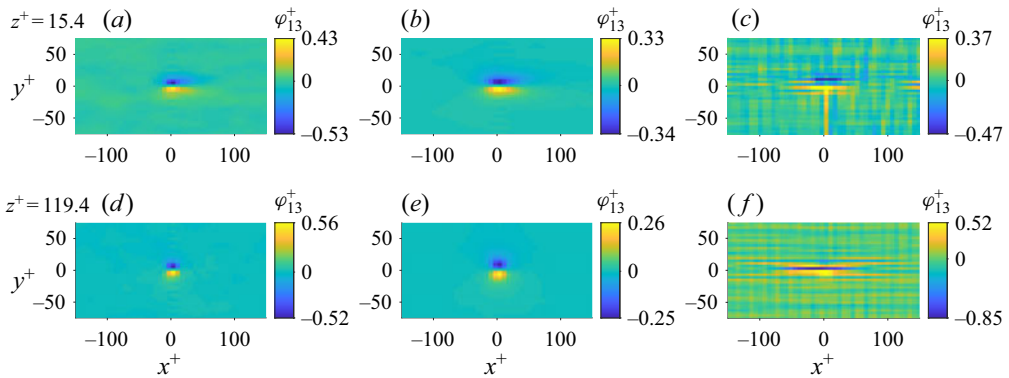
Figure 6. Value of $\varphi_{13}^+(x, y, z; z')$ as a function of x^+ and y^+ for $z^+ = z'^+ = 15.4$ (the first row) and $z^+ = z'^+ = 119.4$ (the second row). The left, middle and right columns correspond to three calculation cases: (*a,d*) calculated by a typical routine with $s = 0.82 \times 10^{-6}\mu_{max}$; (*b,e*) calculated by a typical routine with $s = 0.82 \times 10^{-4}\mu_{max}$; (*c,f*) calculated by a routine neglecting the window-weighting procedure with $s = 0.82 \times 10^{-4}\mu_{max}$.

very large s, the equation system of (4.19) will result in a solution very close to q_{im}, which shows a quite flat pattern in the x–y plane as shown in figure 5. At last, although φ_{13} from case 1 and case 2 shows a clear difference in magnitude, the corresponding reconstructed velocity fields are quite similar. Quantitative examination shows that the averaged *CC* between the reconstructed velocity fields based on the two parameters is approximately 0.995 for two wall-normal positions considered, which validates the robust performance of FLSE.

To quantitatively investigate the influence of s in the reconstruction accuracy, a series of s ranging from $s = 0.82 \times 10^{-7}\mu_{max}$ to $0.82 \times 10^{-1}\mu_{max}$ (logarithmically spaced) are trialled. The minimum s employed in this test is very close to the lower limit for keeping numerical stability. The solved inducing model functions from (4.19) are used to reconstruct a large DNS field (as detailed by table 1) based on (4.12). The *CC*s between reconstructed velocity fields and original velocity fields at three wall-normal positions are displayed in figure 7 as functions of s. The results show that smaller s corresponds to higher reconstruction accuracy, although the results for $s/\mu_{max} < 10^{-3}$ are quite close. The best performance of FLSE achieves a *CC* of larger than 0.9 for all the three velocity components in figures 7(*a*) and 7(*b*), which indicates that the reconstructed velocity field is very similar to the real one. For figure 7(*c*), the reconstruction accuracy is lower since it corresponds to the edge of the reconstructed domain, and only the vortices below this position are considered in the reconstruction. Based on the discussions for figures 6 and 7, this work will adopt $s = 0.82 \times 10^{-4}\mu_{max}$ in the following analysis, which corresponds to a good performance in both convergence and accuracy. It is worthy to point out that the reconstruction results for $s/\mu_{max} < 10^{-3}$ are quite close to each other, and thus prescribing any other s in this range brings no substantial change in the following results of this work.

5.3. *Comparing with the Biot–Savart law*

The Biot–Savart (BS) law provides an explicit formula for reconstructing velocity fields based on vorticity fields. According to Batchelor (1967), the BS law returns the exact velocity fields only if the vorticity has zero normal component at each point of the integration boundary. For wall turbulence, we numerically examined the performance
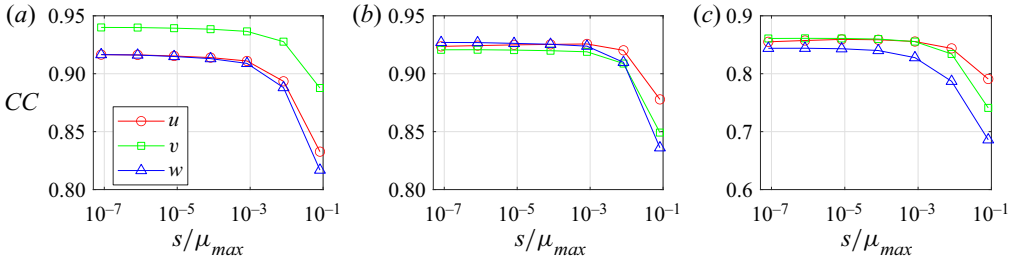
922 A18-20

Figure 7. Correlation coefficients for reconstructed/original velocity fields at $z^+ = 15.4, 119.4, 359.3$ (a-c, respectively) as functions of the regularization parameter.

of the BS law in the vorticity-to-velocity reconstruction, and found its performance is excellent even at the buffer layer ($z^+ = 15.4$): the correlation coefficient between reconstructed and DNS velocity fields is larger than 0.99. This means that the classical BS law works well for the vorticity-to-velocity reconstruction of wall turbulence.

Based on the inherent correlation between vorticity and vortex, the BS law could be employed to reconstruct the velocity field directly based on the vortex field. Several investigators (Perry & Marusic 1995; Marusic 2001; de Silva *et al.* 2016*a*) have employed the BS law to reconstruct wall-bounded turbulence based on the random arrangement of typical vortex tubes. The BS law with respect to the vortex-based reconstruction can be expressed as

$$u(r) = \frac{\mu}{4\pi} \iiint_{\Omega} \frac{\Lambda(r') \times (r - r')}{|r - r'|^3} \, d\Omega. \qquad (5.3)$$

In (5.3), r' is the running position vector for the volume integration and r is the reference position vector; $|\cdot|$ represents the magnitude of the vector quantity in the middle; μ is an artificial multiplier. For vorticity-to-velocity reconstruction, the multiplier equals one by theory. However, for current V2V reconstruction, the multiplier should be adjusted to make the magnitude of reconstructed velocity comparable to the real velocity magnitude. Pirozzoli *et al.* (2010) employed a multiplier of two when dealing with this issue, which was derived based on the situation of a rigidity rotation. In this work, the multiplier is determined by minimizing the mean squares of the deviations between reconstructed results and original DNS results at given wall-normal positions.

For convenience in numerical implementation, (5.3) is reformed as

$$u_i(r) = \iiint_{\Omega} P_{ij}(r - r') \Lambda_j(r') \, d\Omega = P_{ij} * \Lambda_j. \qquad (5.4)$$

Herein, $*$ indicates a 3-D convolution operation, different from the 2-D convolution in (4.12). And the convolution kernel function P_{ij}

$$[P_{ij}] = \frac{\mu}{4\pi(x^2 + y^2 + z^2)^{3/2} + \varepsilon} \begin{bmatrix} 0 & z & -y \\ -z & 0 & x \\ y & -x & 0 \end{bmatrix} \qquad (5.5)$$

where ε is a small parameter, added to avoid the singularity at the origin. In this work, we prescribe $\varepsilon^+ = 10^{-8}$, which makes $P_{ij}(0, 0, 0) = 0$ and brings only a tiny change on the values of P_{ij} at other positions. The convolutional kernel function of the BS law (P_{ij}) resembles the inducing model function φ_{ij} in FLSE. Differently, the BS law employs a fixed and isotropic model function while FLSE adopts a data-driven inducing model,
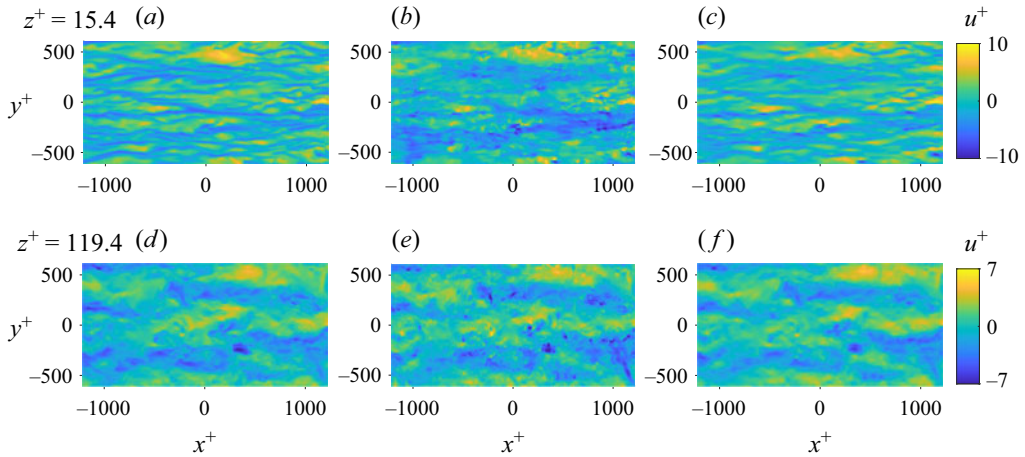
922 A18-21

Figure 8. Instantaneous u^+ fields from $z^+ = 15.4$ (the first row) and $z^+ = 119.4$ (the second row). (a,d) Original DNS data, (b,e) reconstructed u^+ based on the BS law, (c,f) reconstructed u^+ based on FLSE.

which incorporates the statistical imprints of flows. For implementation, P_{ij} is truncated and discretized on the same grid as φ_{ij}.

The reconstructed u fields based on both the BS law and FLSE are displayed in figure 8. The u field displayed in the figure covers an area of $2\delta \times \delta$ in the streamwise–spanwise plane, which is four times as large as the calculation domain of φ_{ij}. Results show that FLSE performs surprisingly well in both the near-wall region and the logarithmic region. The turbulent motions with scales ranging from the spacing of low-speed streaks to the boundary thickness are well recovered. As emphasized in the foregoing discussion, vortices are very sparse in space, and the vortex field contains almost as less information as a scalar field, which poses great challenges for the reconstruction. The success in recovering velocity fields based on vortex structure should be owing to the inherent coherence of vortex structures which could be well modelled as empirical functions as φ_{ij}. The BS law performs as well as FLSE for the logarithmic region but fails to reconstruct the low-speed streaks in the near-wall region. The comparatively poor performance of the BS law in the near-wall region is expected since the distributions of vortices and vorticities are quite different below the buffer layer, as shown in figure 2. The discussion reminds us that the BS law cannot be employed below the logarithmic region for the V2V reconstruction.

Quantitative comparisons between the performances of FLSE and the BS law are provided in figure 9. Figure 9(*a*) shows the *CC*s for reconstructed/original u, v, w as functions of z. The most attractive point indicated from this plot is the good performance of FLSE for $z^+ < 100$. In this region, the *CC*s from FLSE remain a steady variation above 0.9 while the *CC*s from the BS law encounter a dramatic drop for u, v, w. In the logarithmic layer, both FLSE and the BS law perform well, achieving *CC*s of larger than 0.9 for u, v, w. The BS law performs slightly better than LSE for $z^+ > 150$, which supports the application of the BS law in the logarithmic layer (Perry & Marusic 1995; Marusic 2001; de Silva *et al.* 2016*a*) and makes the BS law very competitive in this region considering its simplicity in implementation. The imperfect performance of FLSE for $z^+ > 150$ is attributed to the limited calculation domain for φ_{ij}, which will be further analysed in the following scale-specific assessment. Finally, the performances of both methods deteriorate at the upper boundary of the reconstruction domain, consistent with the results of figure 7.
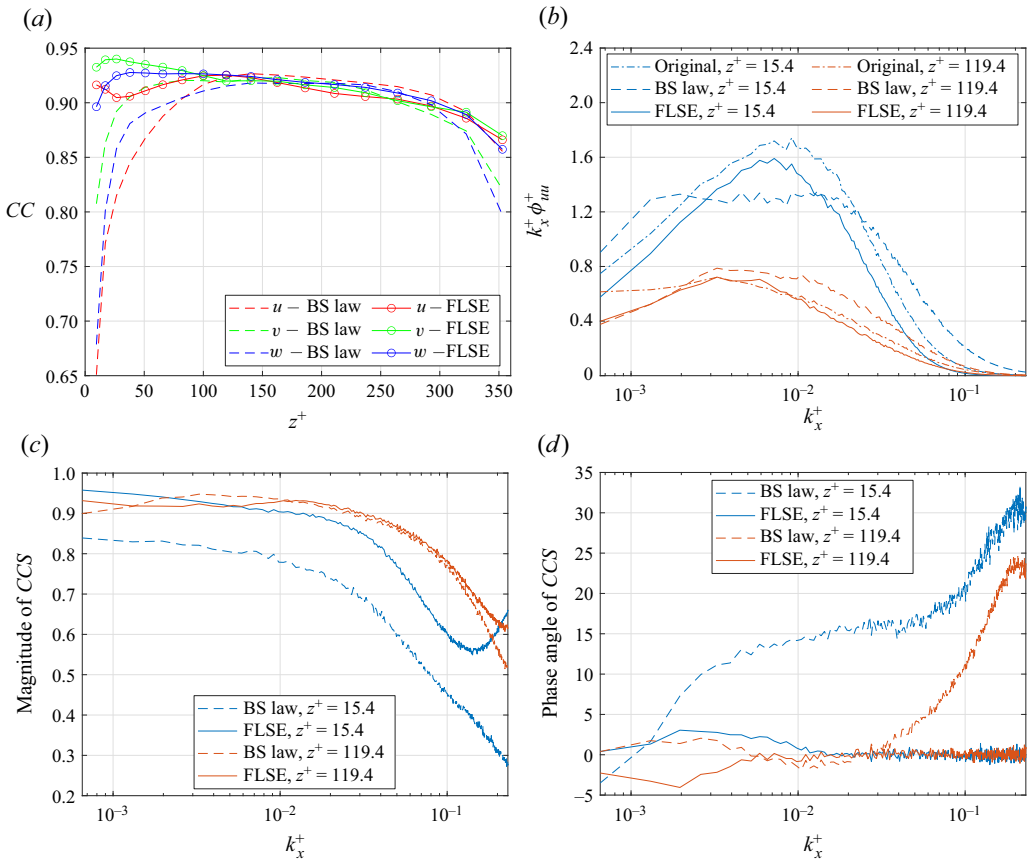
922 A18-22

Figure 9. Quantitative comparisons between the reconstruction results of FLSE and the BS law. (*a*) Correlation coefficients for reconstructed/original fields as functions of z^+; (*b*) premultiplied streamwise energy spectra of u^+ from the original DNS data and the reconstructed results as functions of k_x^+; (*c*) magnitudes of streamwise *CCS* for reconstructed/original u^+; (*d*) phase angles of streamwise *CCS* for reconstructed/original u^+.

The premultiplied spectra shown in figure 9(*b*) provide scale-by-scale comparisons between the reconstructed results and original DNS data. Only the streamwise spectra for the *u* component (denoted as ϕ_{uu}) are taken as examples in this discussion. At $z^+ = 15.4$, the spectra from the BS law show a plateau at $k_x^+ = 1.5 \times 10^{-3} \sim 2 \times 10^{-2}$ (k_x^+ is the streamwise wavenumber), which is obviously different from the prominent peak pattern of the real spectra. The spectra from FLSE show slightly lower energy for all the wavenumbers, but the shape of the spectral curve resembles the real spectra. At $z^+ = 119.4$, the spectra from FLSE are very close to the real spectra except for the very low wavenumbers, where the spectra from both FLSE and the BS law are lower than the real spectra. For high wavenumbers, the spectra from FLSE tend to be lower than the real spectra while the spectra from the BS law tend to be higher to more extent. The results show that FLSE performs better in recovering the energy spectra.

Generally, two signals sharing the same spectra might be quite different since the spectra are integral quantities, which are robust to local events. To further evaluate the reconstruction, the *CCS* between reconstructed and original *u* along the streamwise direction is calculated. As introduced in § 2.3, the magnitude and phase angle of the *CCS* indicate the scale-by-scale correlation degree and scale-by-scale phase deviation

between two input signals, respectively. The *CCS* offers a strict evaluating indicator for the performance of FLSE in reconstructing turbulent motions with different scales. One particular scale deserving more attention is the streamwise length of the calculation domain for φ_{ij} (denoted as L_x), which corresponds to $k_x^+ \approx 5 \times 10^{-3}$.

The magnitudes and phase angles of *CCS* are displayed in figure 9(*c,d*). A lot of information can be drawn from these two plots. Firstly, the overall performance and the effective scale range for FLSE are focused. Figure 9(*c*) shows that for both $z^+ = 15.4$ and $z^+ = 119.4$ the magnitudes of the *CCS* for FLSE-reconstructed/original u remain larger than 0.9 for the scale range of $k_x^+ < 2 \times 10^{-2}$, which corresponds to a bulk of the total energy. The good performance for FLSE is also observed from the phase angles of the *CCS*, which fluctuate in a small range of $\pm 5°$ for the whole wavenumber range considered. The most striking point is that FLSE performs well even for the largest scale considered, which is eight times as large as L_x. Another interesting point is that, for the most part, the *CCS* magnitude decreases with the increase of the wavenumber, which indicates that the large-scale motions are easier to reconstruct than the small-scale fluctuations. This trend is expected since the large structures are composed of large numbers of independent vortex tubes. While the individual vortex tubes suffer from strong random fluctuations, their joint inducing effects are more robust due to the offset effect of independent random fluctuations.

On the other hand, figure 9(*c,d*) also allows a further comparison between FLSE and the BS law. For the results of $z^+ = 15.4$, the advantages of FLSE are observed from both figures 9(*c*) and 9(*d*). FLSE achieves a larger *CCS* magnitude and smaller *CCS* angles for almost all wavenumbers. For the results of $z^+ = 119.4$, the BS law has slightly better performance for $k_x^+ < 10^{-2}$, which corresponds to a length scale of approximately $0.5L_x$. A similar demarcation with $k_x^+ \approx 10^{-2}$ is also observed in the performance of FLSE in figure 9(*d*). For $k_x^+ > 10^{-2}$, the phase angle for the *CCS* fluctuates around zero; yet for $k_x^+ < 10^{-2}$ the phase angle deviates from zero to a negative or positive number. The explanation is clear since the governing equations for φ_{ij} are limited in the calculation domain. The intention of minimizing the reconstruction deviations is not enforced for the scales larger than L_x.

These results constitute an all-round assessment of the reconstruction performance of FLSE and the BS law, which benefits the application of both methods. Mostly, FLSE achieves better reconstruction accuracy, particularly for the buffer layer.

5.4. *Full energy spectra of FLSE-reconstructed TBL*

Figure 10 provides the full pre-multiplied spectra for original velocity fields and the FLSE-reconstructed ones, varying with the wall-normal position. The pre-multiplied streamwise spectra $k_x \phi_{uu}$, $k_x \phi_{vv}$, $k_x \phi_{ww}$ are shown as functions of z and λ_x in the first row, and the pre-multiplied spanwise spectra $k_y \Phi_{uu}$, $k_y \Phi_{vv}$, $k_y \Phi_{ww}$ are displayed as functions of z and λ_y in the second row. Herein, λ_x and λ_y denote the streamwise and spanwise wavelength, respectively; and they are linked to the corresponding wavenumber k_x and k_y by $\lambda_x = 2\pi/k_x$ and $\lambda_y = 2\pi/k_y$. The energy spectra shown here are very consistent with the results of several investigators such as Hutchins & Marusic (2007) for $k_x \phi_{uu}$, Wang *et al.* (2017, 2018) for $k_y \Phi_{uu}$. The spectra from FLSE agree well with the original spectra for the bulk of the total energy. The performance for buffer layer ($z^+ < 80$) is excellent, recovering a satisfying energy distribution for almost the whole scale range considered. The success in the buffer layer is attributed to the relatively smaller inducing range of vortices in this region, which is completely covered in the calculation domain for φ_{ij} as
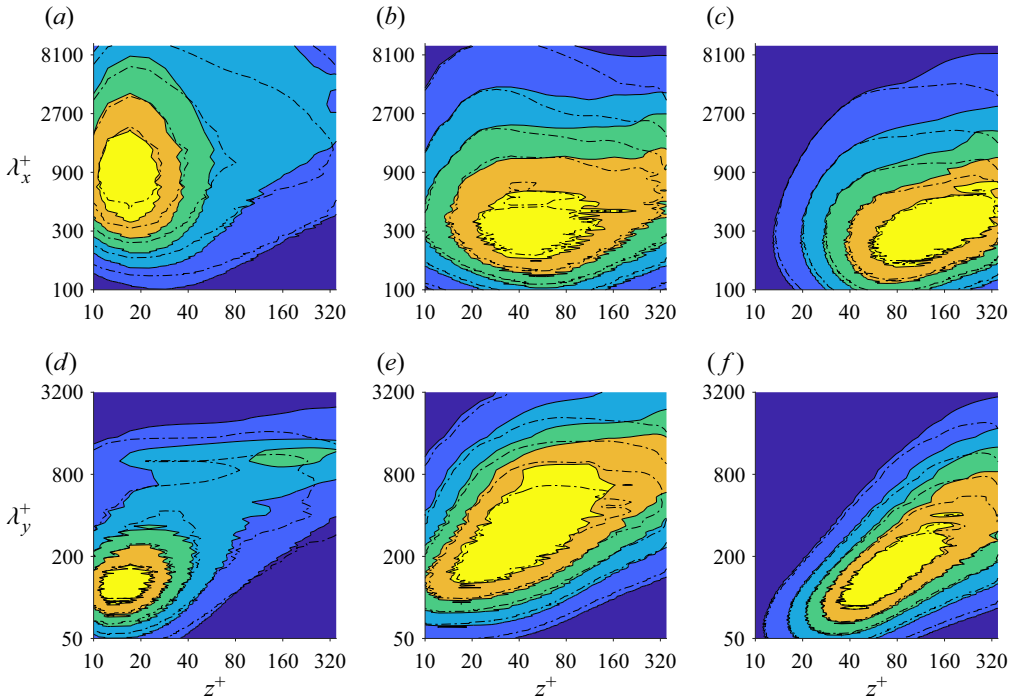
922 A18-24

Figure 10. Contour maps showing the variation of premultiplied spectra for u^+, v^+, w^+ with wall-normal position. The first row: the premultiplied streamwise spectra $k_x^+ \phi_{uu}^+$, $k_x^+ \phi_{vv}^+$, $k_x^+ \phi_{ww}^+$ as functions of z^+ and k_x^+; the second row: the premultiplied spanwise spectra $k_y^+ \Phi_{uu}^+$, $k_y^+ \Phi_{vv}^+$, $k_y^+ \Phi_{ww}^+$ as functions of z^+ and k_y^+. Contour lines show 1/6 to 5/6 of the maximum premultiplied energy, with an increment of 1/6. The shaded and solid contour lines show the results of original DNS data while the dashed contour lines show the results of reconstructed velocity fields based on FLSE.

shown in figure 5. For $z^+ > 80$, deviations between reconstructed spectra and the original spectra are observed for the large scales. Generally, the reconstructed spectra for ϕ_{vv}, ϕ_{ww} are more accurate than those of ϕ_{uu}, which is consistent with the fact that u corresponds to comparatively larger coherence scales. A larger calculation domain of φ_{ij} will account for the structures with larger scales embedded in the logarithmic layer but also significantly burden the calculation resources, which is outside the scope of the work. All in all, the result of FLSE is satisfying for the scale range covered in the current calculation domain.

Energy spectra are among the primary considerations in modelling works of wall-bounded turbulence. To cover the whole scale range of energy spectra, Perry & Marusic (1995) suggested that three types of vortices need to be involved in the vortex model: two types of detached eddies accounting for the largest energy-containing motions and small-scale inertial motions, respectively, and one type of the attached eddy accounting for the self-similar motions in middle scales. As for the representation of the attached eddies, controversy appears. Earlier investigators treated the attached eddies or detached eddies as hierarchies of vortex tubes with Λ or Ω shapes (Perry & Chong 1982) or vortex clusters (del Álamo *et al.* 2006) while recent works tend to recognize them by a pattern of velocities, such as the connected sets of points by Lozano-Durán & Jiménez (2014) and the iso-surface of u by Lee *et al.* (2014) and Yoon *et al.* (2020). Recently, there are also some efforts to extract the contribution of attached eddies from the streamwise spectra of u (Baars & Marusic 2020*a*,*b*; Hu, Yang & Zheng 2020).

Results of figure 10 show that the bulk range of energy spectra can be covered in the induced motions of the vortex fields. Certainly, the contribution of attached eddies could also be attributed to the joint inducing effects of vortex groups. While the vortices with random sizes and strength characterize the local turbulence, the large-scale component of the vortex field explains the large-scale coherent structures (Gad-el-Hak & Bandyopadhyay 1994). The large-scale component of the vortex field might be attributable to the clustered organization of CFSEs (del Álamo *et al.* 2006; Kang *et al.* 2007). Up to present, the modelling works based on random CFSEs are mostly limited to the inertial range for isotropic turbulence (Townsend 1951; Corrsin 1962; Lundgren 1982; Pullin & Saffman 1993). Of particular note is the strained-spiral vortex model proposed by Lundgren (1982), which derives the Kolmogorov spectra based on the randomly oriented collections of non-axisymmetric and strained vortex models. For wall turbulence, the non-isotropy nature and the large-scale coherence hinder the extension of these models. The CFSE-based modelling works should incorporate both the random geometries for individual vortex tubes and the large-scale clustering trend of vortex groups. Perhaps a combination of the attached eddy model with randomly placed vortex tubes could be attempted in future works.

Another topic related to the energy spectra is the inner–outer interaction in wall-bounded turbulence. A lot of investigations (Hutchins & Marusic 2007; Marusic *et al.* 2010; Mathis, Hutchins & Marusic 2011) have shown that large-scale motions in the logarithmic layer have modulation and superposition effects on the velocity fluctuation in the near-wall region. And only the superposition effect contributes to the energy of the near-wall region, accounting for the increasing trend of inner peaks with the increase of the Reynolds number. The superposition effect could be understood as the inducing effect of the vortices at the logarithmic layer, and FLSE allows us to have an insight into this aspect.

In order to separate the inducing effects of vortices from different wall-normal positions on a reference plane, a V2V reconstruction based on height-filtered vortices is performed. Specifically, only the vortices located at a given height range $z \in [z_c - \Delta(z_c), z_c + \Delta(z_c)]$ are considered in the reconstruction of u at the reference plane (e.g. $z_{ref}^+ = 15.4$), and the result is denoted as $u(x, y, z_{ref}; z_c)$. Herein, z_c is the central position for the wall-normal range of the vortices participating in the reconstruction; $\Delta(z_c)$ denotes the half-span, which is set as twice the local interval of the original wall-normal grid. The pre-multiplied streamwise spectra for $u(x, y, z_{ref}; z_c)$ are calculated, which are represented by $k_x \phi_{uu}(k_x, z_{ref}; z_c)$. Contours of $k_x z_c \phi_{uu}(k_x, z_{ref}; z_c)/(2\Delta(z_c))$ are shown as functions of k_x and z_c in logarithmic coordinates in figure 11(*a*), where the multiplier z_c is added to balance the squeezing effect of logarithmic coordinates. Basically, this contour map shows the contribution of vortices at different wall-normal positions to the streamwise spectra of u at the reference plane of $z_{ref}^+ = 15.4$, which are called the contribution spectra for ϕ_{uu} regarding the reference plane of $z_{ref}^+ = 15.4$. Similarly, the contribution spectra for the streamwise spectra of v, w regarding the reference plane of $z_{ref}^+ = 15.4$, and the contribution spectra for the streamwise spectra of u,v,w regarding the reference plane of $z_{ref}^+ = 119.4$ are also calculated and displayed in the first and second rows of figure 11, respectively.

Figure 11 is revealing in several aspects. Firstly, it shows that, compared with figures 11(*b*) and 11(*c*), the contribution spectra for ϕ_{uu} in figure 11(*a*) are flatter along the z_c direction, which indicates the u component is more sensitive to the vortices below or above the reference positions. The sensitivity of u to vortices may be correlated to the lift-up mechanics caused by streamwise vortices, which tends to produce

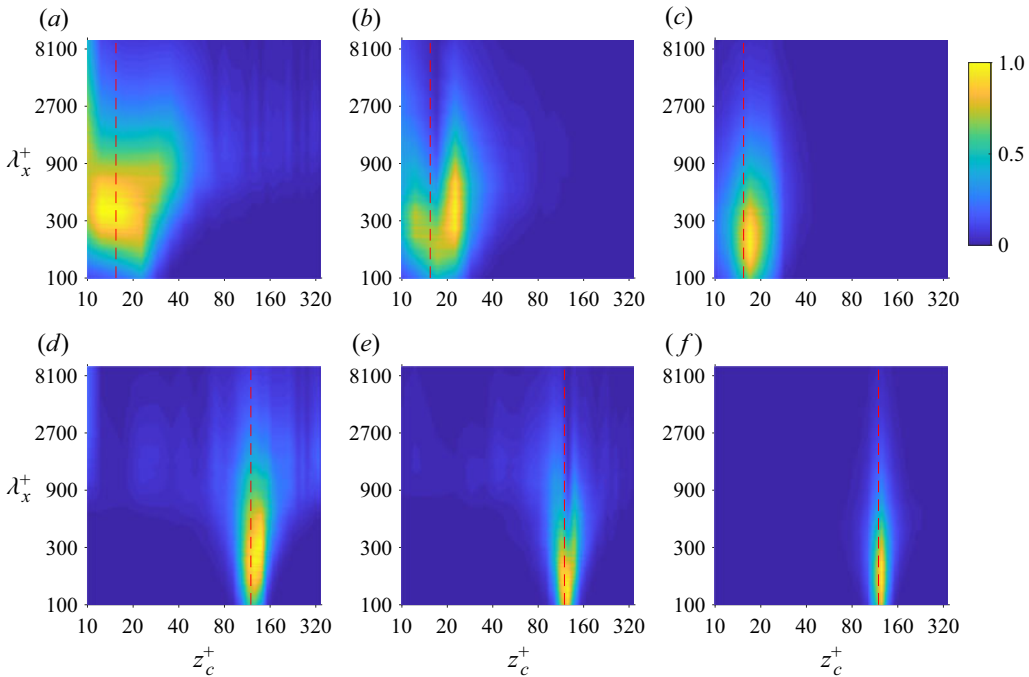Figure 11. Contour maps showing the contribution of vortices at z_c^+ to ϕ_{uu}^+, ϕ_{vv}^+, ϕ_{ww}^+ (*a–f*, respectively) at the reference plane of $z_{ref}^+=15.4$ (the first row) and $z_{ref}^+=119.4$ (the second row), as marked by the red dashed lines. The contours show the local energy contribution premultiplied by $k_x^+ z_c^+$ and normalized by the maximum values.

low-speed structures in the near-wall region (Schoppa & Hussain 2002). In figure 11(*a*), the contribution from $z_c^+ > 100$ can be observed at $\lambda_x > 900$ for ϕ_{uu}, supporting the well-documented superposition effect of large-scale structures on near-wall fluctuations. In figures 11(*b*) and 11(*c*), the energy-contributing regions for ϕ_{vv} and ϕ_{ww} regarding the reference plane of $z_{ref}^+=15.4$ are limited below $z_c^+ < 100$ and $z_c^+ < 50$, respectively. For the contribution spectra regarding the reference plane of $z_{ref}^+=119.4$ (the second row), while the energy-contributing regions for ϕ_{uu} and ϕ_{vv} cover the bulk of the whole wall-normal range considered, the energy-contributing region for ϕ_{ww} remains local. In previous investigations (Woodcock & Marusic 2015), the special behaviour of the w component was also noticed in the scaling law of $\langle w^2 \rangle$, which remains constant in the logarithmic region while both $\langle u^2 \rangle$ and $\langle v^2 \rangle$ show a logarithmic variation with the wall-normal position. The special behaviour of the w component is owing to the bounding effect of the wall, which weakens the inducing effects of vortices on the w component. In fact, the wall-bounding effect was incorporated as the boundary condition in the theoretical works of Perry & Marusic (1995) and Woodcock & Marusic (2015), which yielded the correct scaling law for $\langle u^2 \rangle$, $\langle v^2 \rangle$, $\langle w^2 \rangle$. Figure 11(*f*) provides some evidence for this condition.

5.5. *High-order moments of FLSE-reconstructed TBL*

The energy spectra discussed above only involve the second-order moments of velocities. The higher-order moments offer further indicators to distinguish the reconstructed velocity fields and original DNS velocity fields. This subsection focuses on higher-order moments,
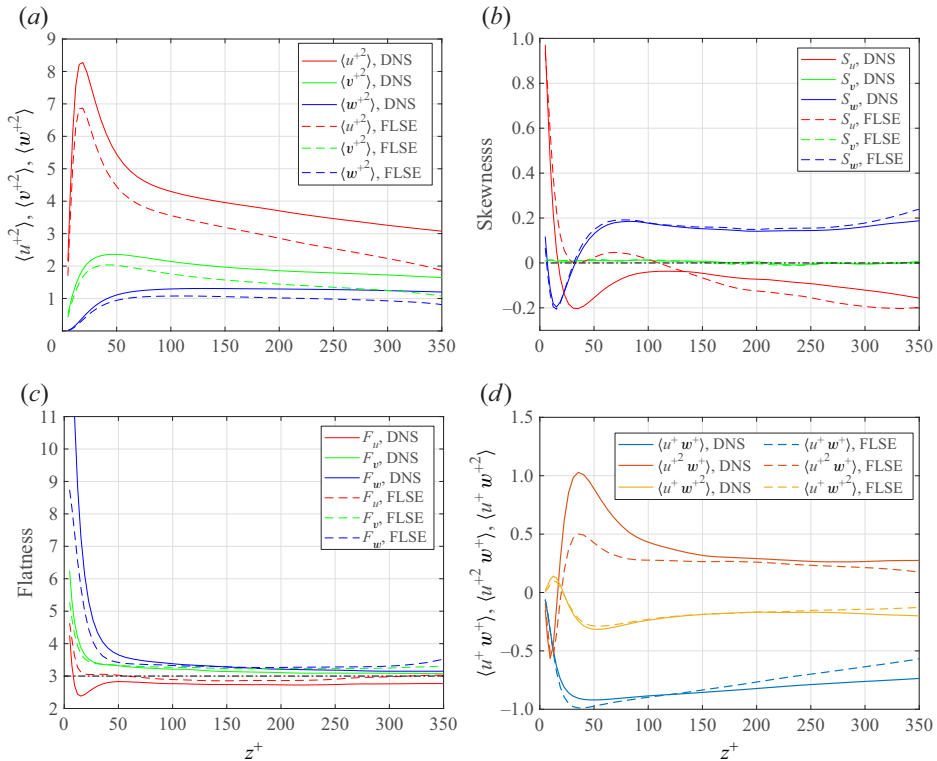
Figure 12. Various moments for u^+, v^+, w^+ as functions of wall-normal positions. (*a*) Fluctuation energy, (*b*) skewness, (*c*) flatness, (*d*) $\langle u^+ w^+ \rangle$ and its wall-normal/streamwise flux quantity ($\langle u^+ w^{+2} \rangle$ and $\langle u^{+2} w^+ \rangle$).

including the skewness and flatness for the three velocity components. The skewness and flatness factors for u (denoted as S_u and F_u) are defined as $\langle u^3 \rangle / \langle u^2 \rangle^{3/2}$ and $\langle u^4 \rangle / \langle u^2 \rangle^2$, respectively. While the skewness factor reflects the asymmetry degree of fluctuating signals, the flatness factor is more correlated to the peaky signals associated with the intermittent turbulence events. Gad-el-Hak & Bandyopadhyay (1994) suggested that the third moment retains the sign information and is more revealing in inferring the characteristics of coherent structures; $\langle u^3 \rangle$ could also be explained as the streamwise flux for the streamwise turbulent energy, and such an explanation is also suitable for $\langle v^3 \rangle$ or $\langle w^3 \rangle$. Besides the moments of individual velocity components, the correlation term $\langle uw \rangle$ (the kinematic Reynolds shear stress with an opposite sign) and its streamwise or wall-normal flux (i.e. $\langle u^2 w \rangle$, $\langle uw^2 \rangle$) (Bandyopadhyay & Watson 1988) are also analysed, considering that they are important terms in the energy balance equation (Bradshaw 1967) or the transportation equations of the shear stress in wall turbulence.

All these statistical quantities from original DNS data and the reconstructed results are shown in figure 12. It shows that the second-order moments from FLSE are lower than the original DNS results, which is consistent with the observations on the energy spectra in figures 9 and 10. As for the skewness and flatness of u (figure 12*b*,*c*), the results from FLSE present distinctive behaviours at the near-wall region compared with the DNS results. For the skewness of u, the FLSE results from $15 < z^+ < 100$ are mostly positive, which are on the opposite of the corresponding DNS results. For the flatness of u, the FLSE results from $15 < z^+ < 50$ stay above or very close to three, while the corresponding

DNS results are always smaller than three. Generally, a positive skewness indicates that the extreme events corresponding to a large fluctuation magnitude are more likely positive, and *vice versa*. A flatness of three is the behaviour of a standard Gaussian distribution, and larger or smaller flatness corresponds to a super-Gaussian or sub-Gaussian behaviour, respectively. It can be inferred from the deviations that the reconstructed u tends to be flatter and contains weak negative fluctuations compared with the original field. In the logarithmic region, the deviations for both skewness and flatness are reduced: both results show a negative skewness and sub-Gaussian behaviour for flatness. Different from the results of u, the skewness and flatness of v, w from FLSE agree well with the original DNS data for the whole wall-normal range considered, which further validates that u poses the most significant challenge for the accurate reconstruction.

The skewness and flatness factors have also been considered in the attached eddy model. The model predicts that the flatness of u, is invariably larger than three (Woodcock & Marusic 2015), which is different from the well-accepted experimental result of 2.8 (Fernholz & Finleyt 1996; Stanislas *et al.* 2008). To build on this aspect, de Silva *et al.* (2016*b*) introduced the spatial exclusion effect in attached eddy model and found that the improved attached eddy model gives a correct prediction on the flatness of u. It validates the importance of the spatial exclusion effect in deriving accurate predictions. The current work reconstructs the velocity fields based on the original vortex fields, which embodies the spatial exclusion effects. The reconstruction results retain the correct behaviour for the flatness of u in the logarithmic layer but not in the near-wall region. This indicates that, besides incorporating the spatial exclusion effect, further reform of the ideal vortex model is needed in order to explain the flatness in the near-wall region.

In figure 12(*d*), the reconstructed results retain the same signs with the corresponding DNS results for all the three quantities, which is promising considering that the sign of $\langle uw^2 \rangle$ could be related to the wall-ward or outward motion induced by dominant vortex structures (Bandyopadhyay & Watson 1988). On the other hand, significant deviations are noticed from the results of $\langle u^2 w \rangle$ at the buffer region. This means that the reconstructed turbulence contains weaker streamwise flux of $\langle uw \rangle$, which might be correlated with the relatively weaker low-speed structures observed in the reconstructed results. The reconstructed $\langle uw \rangle$ has a steeper slope above $z^+ = 50$, resulting in a slightly lower magnitude at the logarithmic region. The discount amount for $\langle uw \rangle$ might be attributable to the very large structures, which are not covered in the domain of the current calculation. Finally, of all the three quantities, the reconstructed results for $\langle uw^2 \rangle$ is most satisfying, it is remarkably consistent with the DNS results.

In order to reveal the reason that FLSE fails to recover the higher-order moments in the near-wall region, the inducing model employed by FLSE needs to be reconsidered. FLSE expressed the inducing effects of vortices as linear operators, which implies that the inducing effects of two vortices with opposite orientations can be modelled by one function with adjustable signs or multipliers. However, the real situation might be more complex, sometimes beyond the capacity of the linear operators. To support this argument, figure 13 shows the conditionally averaged u field around a given positive streamwise vortex at $z^+ = 37.8$, which is calculated by $\langle u(\mathbf{r} + \Delta \mathbf{r}) \Lambda_x^p(\mathbf{r}) \rangle_{\mathbf{r},t}$. Herein, the superscript p indicates a positive-pass filter, which retains positive values of the input field and sets the negative values as zeros. The wall-normal position for the conditional average corresponds to the largest deviation of S_u in figure 12(*b*). As we can see, the u field around a positive vortex shows an asymmetric pattern. In this contour map, the upper side of the central vortex corresponds to negative u with a larger magnitude compared with that from the lower side, which is consistent with the fact that a positive streamwise vortex is distributed
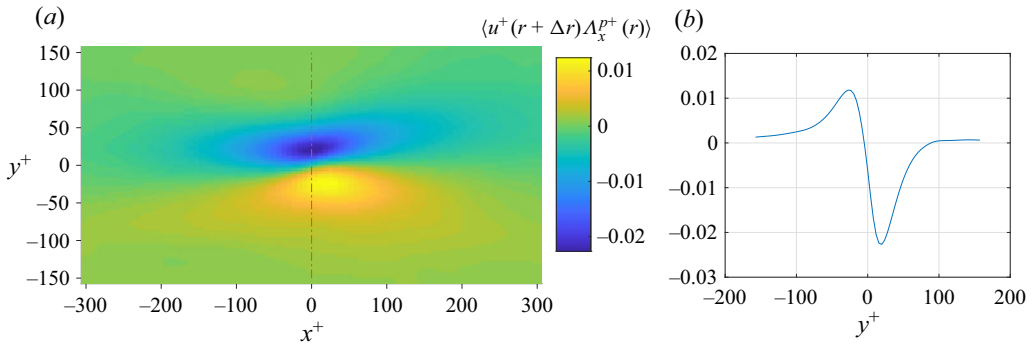
Figure 13. Conditionally averaged u^+ field around a given positive streamwise vortex at $z^+ = 37.8$. (*a*) Contour map of the conditionally averaged u^+ field, (*b*) the conditionally averaged u^+ as a function of y^+ along a line extracted from the contour map, as marked by the red dash-dot line.

below a low-speed streak in this coordinate system. In the implementation of FLSE, the inducing effects of a positive streamwise vortex and a negative streamwise vortex are averaged in one correlation function (as shown in figure 5), which results in a symmetric pattern for inducing models. Such an averaging operation will reduce the intensity of low-speed streaks in reconstructed fields and result in a smaller skewness magnitude and a larger flatness, and also a smaller streamwise flux for $\langle uw \rangle$, which reasonably explains the deviations of the FLSE results displayed by figure 12. To deal with this issue, the reconstruction scheme might be improved by distinguishing the inducing effects of vortices with different signs, which is expected to be the topic of future work.

5.6. *The influence of the λ_{ci}^+ threshold on the reconstructed results*

Recalling the analysis in § 3 of this article, a threshold of λ_{ci}^+ was prescribed to isolate the typical tube-like vortex structures from the vortex fields. Moreover, the correlated discussions about the geometrical properties were mostly limited to these isolated tube-like vortices. In contrast, in the numerical tests of §§ 5.3–5.5, the velocity fields were reconstructed based on the whole vortex fields (Λ), without any threshold. Thus, we need to perform an additional numerical test involving the influence of the threshold issue, with the purpose of bridging the divide between the discussions about the isolated vortex tubes and the V2V reconstruction results in §§ 5.3–5.5.

To show the isolated vortices for prescribed thresholds, figure 14 provides the contour maps for the vortex strength (λ_{ci}^+) at two wall-normal positions. Two sets of contour lines for $\lambda_{ci}^+=0.05$ and $\lambda_{ci}^+=0.1$ are highlighted by the solid lines with different colours. As we can see, the λ_{ci}^+ field presents a visually fragmented pattern. Most of the isolated vortices have a thickness of less than 50 wall units. Comparatively, $\lambda_{ci}^+=0.1$ recognizes stronger and finer vortex cores, which covers only a small portion of the total area. The iso-surfaces of $\lambda_{ci}^+=0.1$ were used to display the vortex tubes in figure 2. It is close to the threshold of $\lambda_{ci}^+=0.08$ employed by Jodai & Elsinga (2016), also for the vortex visualization purposes. On the other hand, for the sake of extracting the vortex properties, such as the radius or circulation, investigators tended to use smaller thresholds in order to count in the low-swirl regions surrounding the vortex cores. For example, Ganapathisubramani *et al.* (2006) and Gao *et al.* (2011) adopted a threshold of approximately 0.035 in their investigations, close to $\lambda_{ci}^+=0.05$ shown in the contour maps. Outside the solid lines, weak vortices with
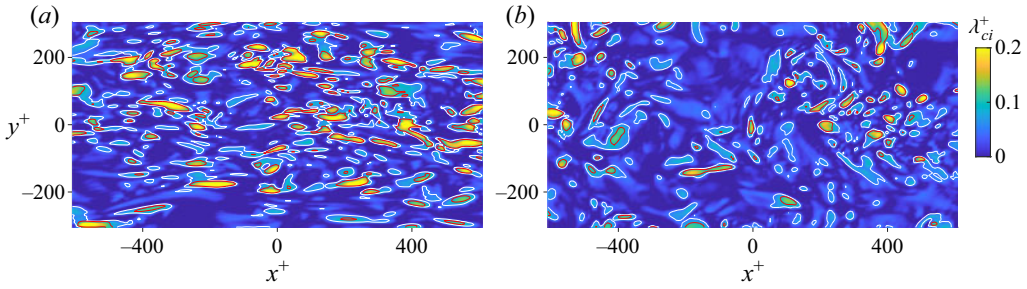
922 A18-30

Figure 14. The contour maps of the vortex strength (λ_{ci}^+) in the streamwise–spanwise plane at $z^+ = 15.4$ (*a*) and $z^+ = 119.4$ (*b*). Two sets of contour lines for $\lambda_{ci}^+ = 0.05$ and $\lambda_{ci}^+ = 0.1$ are highlighted by white and red lines, respectively.

$\lambda_{ci}^+ < 0.05$ can also be observed in the contour maps. These weak vortices are usually disregarded in experimental investigations because they are vulnerable to measurement uncertainties. However, their roles in the V2V reconstruction might be non-negligible since they cover a large portion of the total area and have larger scales.

Based on these discussions, we will trial three specially filtered vortex fields in the V2V reconstructions: (a) the weak vortex fields $\boldsymbol{\Lambda}_W$, obtained by retaining the vortex vectors satisfying $\lambda_{ci}^+ < 0.05$ and setting all the other vortex vectors as zeros; (b) the strong vortex fields $\boldsymbol{\Lambda}_{S1}$, acquired by filtering the original vortex fields based on the criterion $\lambda_{ci}^+ \geq 0.05$; and (c) the strong vortex fields $\boldsymbol{\Lambda}_{S2}$, acquired by filtering original vortex fields based on $\lambda_{ci}^+ \geq 0.1$. The original vortex fields without any filtering process are denoted as $\boldsymbol{\Lambda}_O$. Obviously, the above definitions yield that $\boldsymbol{\Lambda}_O = \boldsymbol{\Lambda}_W + \boldsymbol{\Lambda}_{S1}$.

In the following numerical tests, the velocity fields are separately reconstructed based on $\boldsymbol{\Lambda}_W$, $\boldsymbol{\Lambda}_{S1}$ or $\boldsymbol{\Lambda}_{S2}$ using the same method with the previous reconstruction for $\boldsymbol{\Lambda}_O$. Specifically, a convolution operation is performed on these vortex fields, and the kernel functions are the inducing model functions (φ_{ij}) calculated in § 5.2. The reconstruction formula could be found in (4.12), where the input vortex fields should be replaced accordingly. To make it convenient for the following discussions, the reconstructed streamwise velocity components based on $\boldsymbol{\Lambda}_O$, $\boldsymbol{\Lambda}_W$, $\boldsymbol{\Lambda}_{S1}$ and $\boldsymbol{\Lambda}_{S2}$ are represented by $u_{O,rec}$, $u_{W,rec}$, $u_{S1,rec}$ and $u_{S2,rec}$, respectively. The original streamwise velocity component from the DNS data is represented by u_{DNS}. Based on the linear property of the reconstruction, we can derive $u_{O,rec} = u_{W,rec} + u_{S1,rec}$ from $\boldsymbol{\Lambda}_O = \boldsymbol{\Lambda}_W + \boldsymbol{\Lambda}_{S1}$. The linear reconstruction also implies that $u_{W,rec}$, $u_{S1,rec}$ and $u_{S2,rec}$ reflect the separate contributions of $\boldsymbol{\Lambda}_W$, $\boldsymbol{\Lambda}_{S1}$ and $\boldsymbol{\Lambda}_{S2}$ in the $\boldsymbol{\Lambda}_O$-based reconstruction results ($u_{O,rec}$).

Table 2 collected some statistical information about $\boldsymbol{\Lambda}_W$, $\boldsymbol{\Lambda}_{S1}$, $\boldsymbol{\Lambda}_{S2}$ and their reconstruction results. The third column of this table provides the volume fractions corresponding to different vortex fields, defined by the ratio of the volumes occupied by the selected vortices (with non-zero magnitudes) to the total volume considered. The fourth and fifth columns give the mean squares of the reconstructed u, i.e. $\langle u_{M,rec}^2 \rangle$, $\langle u_{S1,rec}^2 \rangle$ and $\langle u_{S2,rec}^2 \rangle$ (collectively denoted as $\langle u_{\cdot,rec}^2 \rangle$) at $z^+ = 15.4$ and $z^+ = 119.4$, respectively. The last two columns provide the correlation coefficients between the reconstructed u and u_{DNS} at the same wall-normal positions.

Among the three kinds of vortex field, $\boldsymbol{\Lambda}_W$ owns the largest volume factions, occupying nearly half of the total volume. The correlation coefficient between $u_{W,rec}$ and u_{DNS} at $z^+ = 15.4$ is as large as 0.83, which is the largest among these results. But at $z^+ = 119.4$, the corresponding correlation coefficient decreases to 0.77, much lower than that of $\boldsymbol{\Lambda}_{S1}$.

Vortex field	Threshold	Volume fraction of the vortices	$\langle u_{\cdot,rec}^{+2} \rangle$		Correlation coefficient	
			$z^+ = 15.4$	$z^+ = 119.4$	$z^+ = 15.4$	$z^+ = 119.4$
Λ_W	$\lambda_{ci}^+ < 0.05$	45.2 %	0.958	0.440	0.830	0.772
Λ_{S1}	$\lambda_{ci}^+ \geq 0.05$	18.6 %	3.80	2.00	0.826	0.861
Λ_{S2}	$\lambda_{ci}^+ \geq 0.1$	5.08 %	1.67	0.764	0.672	0.724

Table 2. Statistical information about different vortex fields and their reconstruction results.
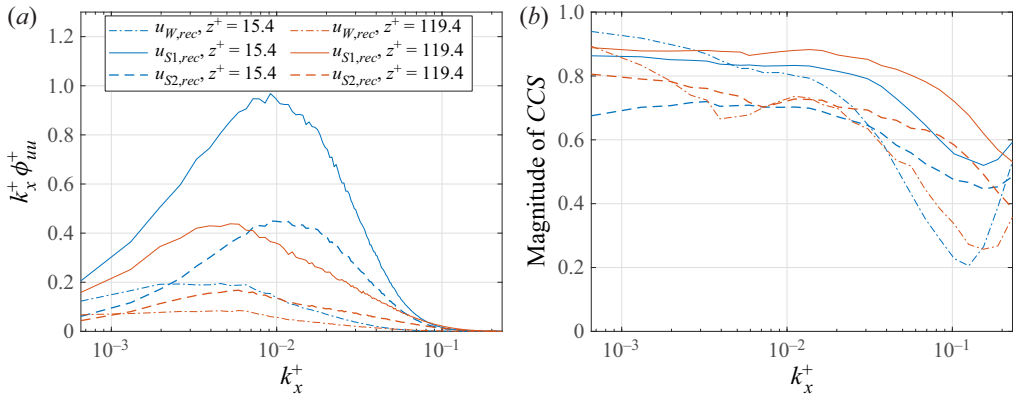
Figure 15. Spectral analysis on $u_{W,rec}$, $u_{S1,rec}$ and $u_{S2,rec}$. (*a*) The premultiplied energy spectra for $u_{W,rec}$, $u_{S1,rec}$ and $u_{S2,rec}$; (*b*) the magnitude of streamwise *CCS* between u_{DNS} and $u_{\cdot,rec}$ (including $u_{W,rec}$, $u_{S1,rec}$ and $u_{S2,rec}$).

In contrast to Λ_W, the volume fraction for Λ_{S2} is only approximately 5 %, the lowest among the three vortex fields. The shortcoming in volume faction causes the lowest reconstruction correlation coefficients for Λ_{S2}. Compared with Λ_W, the advantage of Λ_{S2} for the V2V reconstruction is in the vortex strength. Stronger vortices induce larger fluctuation magnitudes, which explains why $\langle u_{S2,rec}^2 \rangle$ is much larger than $\langle u_{M,rec}^2 \rangle$; Λ_{S1} has a volume fraction three times larger than that of Λ_{S2} and contains more strong vortices, which make it achieve larger $\langle u_{S1,rec}^{+}{}^2 \rangle$ and correlation coefficients at the same time. The data in the table also reflect the trend that the reconstruction accuracy drops with the increase of the filtering threshold.

Figure 15(*a*) shows the premultiplied energy spectra for $u_{W,rec}$, $u_{S1,rec}$ and $u_{S2,rec}$. At first glance, we can see the integral energy of $u_{S1,rec}$ is much larger than that of $u_{W,rec}$ or $u_{S2,rec}$, consistent with the $\langle u_{\cdot,rec}^2 \rangle$ data shown in table 2. Both the spectra of $u_{S1,rec}$ and $u_{S2,rec}$ present obvious peaks at $k_x^+ \approx 10^{-2}$ and $k_x^+ \approx 6 \times 10^{-3}$, for $z^+ = 15.4$ and $z^+ = 119.4$, respectively. But for the spectra of $u_{W,rec}$, the curve shows a plateau at $k_x^+ < 7 \times 10^{-3}$. The distribution of the spectra for $u_{W,rec}$ indicates that it spares a larger proportion of the total energy for small wavenumbers. Particularly for the results at $z^+ = 15.4$, the curve for $u_{W,rec}$ is above that of $u_{S2,rec}$ at $k_x^+ < 2 \times 10^{-3}$. However, for the spectra of larger wavenumbers, the contribution from Λ_W is much lower compared with Λ_{S1} and Λ_{S2}.

The magnitude of the streamwise *CCS* between u_{DNS} and the corresponding reconstructed result ($u_{W,rec}$, $u_{S1,rec}$ or $u_{S2,rec}$) is displayed in figure 15(*b*). As mentioned in § 2, the *CCS* magnitude provides the scale-by-scale correlation degree between two input

velocity fields. As shown by figure 15(b), the *CCS* magnitude for $u_{S1,rec}$ stays above 0.8 for $k_x^+ < 3 \times 10^{-2}$ and the corresponding curve shows a decreasing trend with the increase of wavenumbers. The *CCS* magnitude for $u_{S2,rec}$ is obviously lower than that of $u_{S1,rec}$ for all the wavenumbers considered, presenting a decreasing trend similar to the curve for $u_{S1,rec}$. Comparatively, the curves for $u_{W,rec}$ decrease faster than those of $u_{S1,rec}$ or $u_{S2,rec}$. At $z^+ = 15.4$, the curve for $u_{W,rec}$ stays above 0.9 for $k_x^+ < 10^{-3}$, achieving the largest *CCS* magnitude. However, for $k_x^+ > 3 \times 10^{-2}$, the curve for $u_{W,rec}$ drops below that of $u_{S2,rec}$, which is the lowest.

To summarize, Λ_{S1} contributes significantly to the bulk energy spectra and the corresponding *CCS* magnitudes maintain high levels for a wide wavenumber range; Λ_W mainly builds on the low-wavenumber spectra, and its contribution is more prominent in the near-wall region. This indicates that the large-scale velocity structures could be formed by the joint inducing effects of the clusters containing both weak vortices and stronger vortices. The advantage of Λ_W for smaller wavenumbers might be attributable to the larger volume fraction, which means more vortex vectors participating in the reconstructions.

Besides Λ_W and Λ_{S1}, the performance of Λ_{S2} deserves more attention because the vortex tubes corresponding to Λ_{S2} have been highlighted for the geometrical property in § 3 of this work. The above tests show that the spectrum of $u_{S2,rec}$ is much lower than that of $u_{S1,rec}$ and the corresponding *CCS* magnitudes for most wavenumbers are approximately 0.7, which is not satisfying. It is important to keep in mind that the above tests emphasized the separate contributions of Λ_W, Λ_{S1} and Λ_{S2} to the total (Λ_O-based) reconstruction. Specifically, the inducing model functions used in the above reconstructions were obtained in § 5.2 for the purpose of Λ_O-based reconstruction. Therefore, the above results cannot reflect the utmost ability of Λ_{S2} in independently reconstructing the original velocity fields. To determine this, we need to recalculate the inducing model functions based on the correlation functions of Λ_{S2} and u_{DNS}.

Based on these considerations, we will refine the reconstruction based on Λ_{S2} via the standard FLSE. Firstly, the correlation function of $R_{jm} = \langle \Lambda_{S2,j} \Lambda_{S2,m} \rangle$ and $q_{im} = \langle \Lambda_{S2,i} u_{DNS,m} \rangle$ are statistically calculated. Then, equations (4.13) are solved by using the FFT scheme, which returns new inducing model functions $\varphi_{S2,ij}$. The regularization parameter s is prescribed as the same value as that used in § 5.2. At last, the reconstructed velocity fields are obtained by (4.12). To make a distinction with the former reconstructed result ($u_{S2,rec}$), we denote the newly reconstructed u (via the standard FLSE) as $u_{S2,FLSE}$.

Figures 16(a) and 16(b) shows the contour maps for $u_{S2,FLSE}$ at $z^+ = 15.4$ and $z^+ = 119.4$. These maps can be compared with the contour maps of u_{DNS} shown in figure 8. To facilitate the comparison, we overlay the contour maps in figure 16(a,b) with the contour lines of $u_{DNS} = 0$. As can be seen from the maps, while the low-speed streak in $u_{S2,FLSE}$ is weaker than that of u_{DNS} (in figure 8), the larger flow patterns are reasonably consistent. Comparatively, $u_{S2,FLSE}$ for $z^+ = 119.4$ is more consistent with u_{DNS}. The premultiplied spectra for $u_{S2,FLSE}$ and u_{DNS} are shown in figure 16(c). At $z^+ = 119.4$, the curve for $u_{S2,FLSE}$ is close to that of u_{DNS} nearby the peak position ($k_x^+ = 3 \times 10^{-3} \sim 4 \times 10^{-3}$), which corresponds to a length scale of $1.3\delta \sim 1.7\delta$. This implies that the large-scale motions in the logarithmic region could be approximately explained as the inducing effects of the strong vortices. For smaller wavenumbers of $k_x^+ < 2 \times 10^{-3}$, the deviations between the spectra of $u_{S2,FLSE}$ and u_{DNS} become larger. This might be attributable to the limited calculation domain for solving the inducing functions, as we discussed in § 5.1. At $z^+ = 15.4$, the maximum magnitude of the spectrum of $u_{S2,FLSE}$ is approximately 30 % lower than that of u_{DNS}. The worse performance in the near-wall region could be caused by the viscous diffusion effect, which makes the vortex distribution not as concentrated
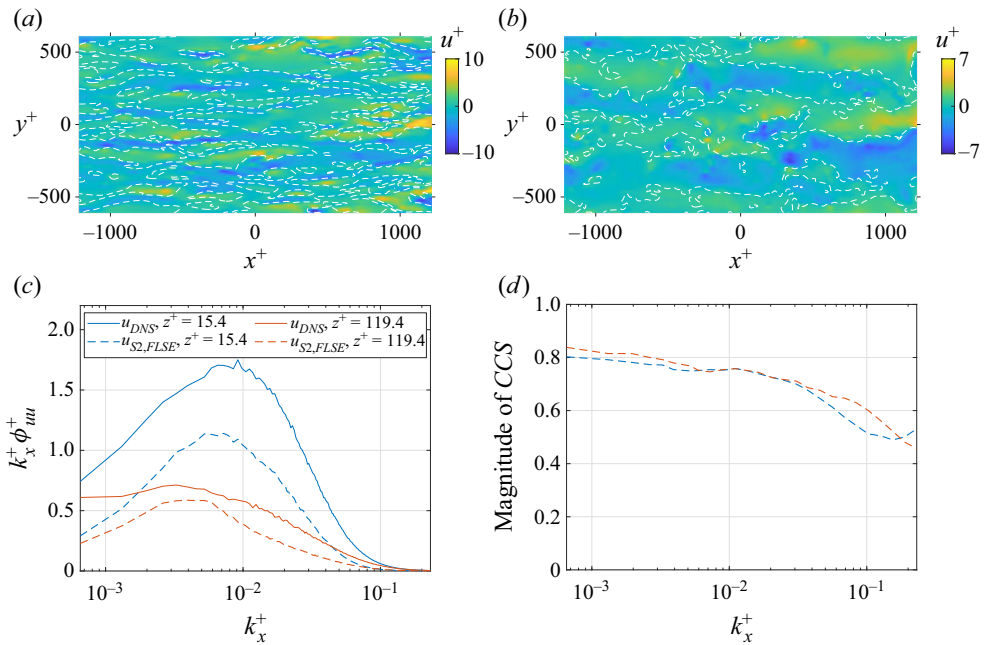
Figure 16. The reconstructed results based on Λ_{S2} via the refined reconstruction strategy. (*a*–*b*) The contour maps of $u_{S2,FLSE}$ at $z^+ = 15.4$ and $z^+ = 119.4$, respectively. To provide a reference, the contour lines of $u_{DNS} = 0$ are also shown by the white dashed lines. (*c*) The premultiplied energy spectra for $u_{S2,FLSE}$ and u_{DNS}. (*d*) The magnitude of streamwise *CCS* between $u_{S2,FLSE}$ and u_{DNS}.

as that in the logarithmic region. Thus, a smaller threshold should be adopted to count in more regions around the vortex centres. Comparing the spectra shown in figures 16(*c*) and 15(*a*), we can see that the refined reconstruction scheme significantly improves the spectrum magnitude. The magnitude of streamwise *CCS* between $u_{S2,FLSE}$ and u_{DNS} is provided in figure 16(*d*). The improvement brought by the refined reconstruction strategy can also be found by comparing the curves in figure 16(*d*) with those in figure 15(*b*). For the wavenumber range of $k_x^+ < 10^{-2}$ ($\lambda_x^+ > 0.52\delta^+$), the curves in figure 16(*d*) stay at the level of 0.75–0.8. The results are mostly encouraging since these vortices participating in the reconstruction only occupy 5 % of the volume considered. It demonstrates that the strong tube-like vortices are theoretically important for explaining the large-scale motions in TBL.

6. Concluding remarks

Vortices are frequently viewed as the building blocks of turbulence. The current investigation contributed to the topic of how to use these building blocks to construct a wall-turbulence flow. For investigation convenience, the vortex was defined by a combination of the swirl strength and the real eigenvector of the velocity gradient tensor. The alignment of vortex iso-surface and vortex orientation was quantitatively analysed by using the differential geometry, which supports the current vortex definition. FLSE was proposed to accomplish the V2V reconstruction. The new method was comprehensively compared with the classical BS law from the respect of correlation coefficients, the energy spectra and the complex coherence spectra for reconstructed/original velocity fields.

For the most part, the new method performed better than the BS law, especially for the buffer region.

The reconstruction method was employed to investigate the inducing effects of vortices in TBL, which yielded several revealing implications. Firstly, the bulk of the energy spectra can be covered by the induced motions of vortices. The superposition effect of large-scale motions from the logarithmic region on the near-wall fluctuations can also be interpreted as the vortex-inducing effects. Comparatively, the energy spectra of u are more vulnerable to the inducing effects of vortices below or above the reference plane. The energy contribution region for the w spectra is limited at the neighbouring region of the reference height, which is attributable to the bounding effect of the wall.

Secondly, the high-order moments of u are highly correlated with the asymmetric inducing effects of a vortex with a positive/negative sign, which is beyond the capacity of a linear reconstruction scheme (FLSE). In the implementation of FLSE, the inducing effects of positive vortices and negative vortices were averaged in one correlation function, which resulted in a symmetric pattern for inducing models. It is expected that the reconstruction method might be further improved by using nonlinear inducing models and distinguishing the inducing effects of vortices with opposite orientations.

Thirdly, the strong vortices and weak vortex components play different roles in the V2V reconstruction. While the strong vortex components contribute to the bulk scale range of the spectra, the weak vortex components mainly contribute to the low-wavenumber spectra. A refined reconstruction based on the strongest vortices (occupying 5 % of the total volume) returned a velocity field sharing a high correlation degree with the DNS field. The main flow features of TBL, including both the near-wall streaks and large-scale motions, can be explained by the inducing effects of strong tube-like vortices.

It should be recalled that the FFT implementation of FLSE only works for the flows which have homogeneous directions. The canonical turbulent channel flow and the TBL in a limited streamwise range present homogeneous in the wall-parallel planes, which are suitable for using the FFT method. For general 3-D flow fields, the reconstruction calculation could be quite expensive if the FFT method cannot be employed. Another thing that needs to be addressed is the definition of the vortex field. Although § 3 provided some support for this definition, the question about the optimal definition for vortex regarding the V2V reconstruction remains open, which might be further investigated in future work.

Declaration of interests. The authors report no conflict of interest.

Author ORCIDs.

 Chengyue Wang https://orcid.org/0000-0003-2526-411X;

 Qi Gao https://orcid.org/0000-0002-2532-0997;

 Jinjun Wang https://orcid.org/0000-0001-9523-7403.

Appendix A. Principal directions of local curvatures

Following the conventions in this article, the vortex magnitude field is designated by $\lambda_{ci}(\boldsymbol{r})$. Focus on the neighbourhood of a given point $\boldsymbol{r}_0$, and let $\delta\boldsymbol{r} = \boldsymbol{r} - \boldsymbol{r}_0$ denote the relative

position vector regarding r_0 ($|\delta r| = |r - r_0| \ll 1$). According to Taylor's theorem, $\lambda_{ci}(r)$ could be approximated as a quadrant form, as

$$\lambda_{ci}(r) = \lambda_{ci}(r_0) + \delta r^T G + \tfrac{1}{2}\delta r^T H \delta r + o(\delta r^2), \tag{A1}$$

where $G = \nabla \lambda_{ci} = [\partial \lambda_{ci}(r_0)/\partial x, \partial \lambda_{ci}(r_0)/\partial y, \partial \lambda_{ci}(r_0)/\partial z]^T$ denotes the gradient of $\lambda_{ci}(r)$, and

$$H = \begin{bmatrix} \dfrac{\partial^2 \lambda_{ci}(r_0)}{\partial x^2} & \dfrac{\partial^2 \lambda_{ci}(r_0)}{\partial x \partial y} & \dfrac{\partial^2 \lambda_{ci}(r_0)}{\partial x \partial z} \\[2ex] \dfrac{\partial^2 \lambda_{ci}(r_0)}{\partial x \partial y} & \dfrac{\partial^2 \lambda_{ci}(r_0)}{\partial y^2} & \dfrac{\partial^2 \lambda_{ci}(r_0)}{\partial y \partial z} \\[2ex] \dfrac{\partial^2 \lambda_{ci}(r_0)}{\partial x \partial z} & \dfrac{\partial^2 \lambda_{ci}(r_0)}{\partial y \partial z} & \dfrac{\partial^2 \lambda_{ci}(r_0)}{\partial z^2} \end{bmatrix}, \tag{A2}$$

which is the so-called Hessian matrix.

The principal directions for local curvatures should be searched in the tangent plane of local vortex surface. Thus we impose a constrain that δr should be a vector in the tangent plane of the local vortex surface, which means

$$G^T \delta r = 0. \tag{A3}$$

Any δr satisfying (A3) can be expressed as

$$\delta r = \alpha_1 e_1 + \alpha_2 e_2 = [e_1, e_2][\alpha_1, \alpha_2]^T = E\alpha, \tag{A4}$$

where e_1, e_2 are two orthogonal unit vectors satisfying

$$G^T e_1 = G^T e_2 = 0, \tag{A5}$$

and α could be any real vector indicating a direction in the tangent plane.

Under this constrain of (A3) and employing the representation of (A4), it can be derived that

$$\lambda_{ci}(r) = \lambda_{ci}(r_0) + \tfrac{1}{2}\alpha^T E^T H E \alpha + o(\delta r^2). \tag{A6}$$

Now consider the variation of λ_{ci} along one direction in the tangent plane of the vortex surface, which can be achieved from (A6) by linearly changing α, i.e. $\alpha = \alpha_0 t$. Herein, α_0 is a given unit direction vector and t is a variable parameter. Obviously, λ_{ci} varies with t as a parabolic curve. The principal directions correspond to the directions with the largest and smallest curvatures for $\lambda_{ci}(t)$, which is equivalent to the eigenvalue problem of $E^T H E$. Let v_1 and v_2 denote the eigenvectors for $E^T H E$, corresponding to two eigenvalues of $\mu_1, \mu_2 (\mu_1 > \mu_2)$, respectively. Then, the first and second principal directions for the local curvatures at r_0 should be $\delta r_1 = E v_1$ and $\delta r_2 = E v_2$.

Appendix B. Deducing (4.4) from (4.3)

For simplicity, rewrite the deviation D in the form of inner product, i.e.

$$D = \iiint_\Omega (\hat{u}_i - u_i)(\hat{u}_i - u_i) \, d\Omega \Big/ \iiint_\Omega d\Omega = (\hat{u}_i - u_i, \hat{u}_i - u_i), \tag{B1}$$

where $(\cdot, \cdot)$ represents the inner product of the two terms separated by the comma. The repeated index i of the two bracketed terms implies an automatic summation, following Einstein's summation convention.

To find $\mathcal{L}_{ij}$ which results in the minimum $\langle D \rangle$, give a small variation (δ) on $\mathcal{L}_{ij}$ and investigate the corresponding variation of $\langle D \rangle$. Thus we have

$$\delta \langle D \rangle = \delta \langle (\hat{u}_i - u_i, \hat{u}_i - u_i) \rangle = 2 \langle (\hat{u}_i - u_i, \delta \hat{u}_i) \rangle. \tag{B2}$$

Note that the implicit position vector is $\boldsymbol{r}$ for $\hat{u}_i, u_i, \delta \hat{u}_i$. According to the calculus of variations, the minimum of $\langle D \rangle$ corresponds to a balanced position, where for any possible variation of $\mathcal{L}_{ij}$, the corresponding variation of $\langle D \rangle$ should be zero, i.e.

$$\delta \langle D \rangle = 2 \langle (\hat{u}_i - u_i, \delta \hat{u}_i) \rangle = 0 \text{ for any possible } \delta \hat{u}_i = \delta (\mathcal{L}_{ij}) \Lambda_j. \tag{B3}$$

Now, let $\delta \hat{u}_i = \delta \mathcal{L}_{ij} \Lambda_j = \Lambda_m(\boldsymbol{r}') \delta(\boldsymbol{r} - \boldsymbol{r}'') \delta_{in}$, where $\delta(\boldsymbol{r} - \boldsymbol{r}'')$ is the 3-D Dirac delta function and δ_{in} is the three-order Kronecker delta. $\boldsymbol{r}', \boldsymbol{r}''$ could be any reference position vectors and m, n are indices varying from one to three. The specific definitions for $\delta(\boldsymbol{r} - \boldsymbol{r}'')$ and δ_{in} could be indicated by

$$(f(\boldsymbol{r}), \delta(\boldsymbol{r} - \boldsymbol{r}'')) = \iiint_{\Omega} f(\boldsymbol{r}) \delta(\boldsymbol{r} - \boldsymbol{r}'') \, \mathrm{d}\Omega = f(\boldsymbol{r}''), \tag{B4}$$

where $f(\boldsymbol{r})$ could be any 3-D continuous function, and

$$\delta_{in} = \begin{cases} 0 & \text{if } i \neq n \\ 1 & \text{if } i = n \end{cases}. \tag{B5}$$

The prescription for the form of $\delta \hat{u}_i$ is based on two considerations. First, the form should facilitate an effective simplification for the form of $\delta \langle D \rangle$. Second, the form should have sufficient variations by adjusting the involved indices or parameters, in order to obtain enough equations for the unknown $\mathcal{L}_{ij}$. Here,
$\delta \hat{u}_i = \delta \mathcal{L}_{ij} \Lambda_j = \Lambda_m(\boldsymbol{r}') \delta(\boldsymbol{r} - \boldsymbol{r}'') \delta_{in}$ implies a possible variation for $\mathcal{L}_{ij}$, which results in a variation of $\langle D \rangle$ as

$$\delta \langle D \rangle = 2 \langle (\hat{u}_i - u_i, \Lambda_m(\boldsymbol{r}') \delta(\boldsymbol{r} - \boldsymbol{r}'') \delta_{in}) \rangle = 0. \tag{B6}$$

Simplifying this equation by using (B4) and (B5) gives

$$\langle (\hat{u}_i - u_i, \Lambda_m(\boldsymbol{r}') \delta(\boldsymbol{r} - \boldsymbol{r}'') \delta_{in}) \rangle = \langle (\hat{u}_n(\boldsymbol{r}'') - u_n(\boldsymbol{r}'')) \Lambda_m(\boldsymbol{r}') \rangle = 0. \tag{B7}$$

In the following equations, $\boldsymbol{r}''$ is neglected for simplicity. Considering that $\hat{u}_n = \mathcal{L}_{nj} \Lambda_j$, we have

$$\langle (\mathcal{L}_{nj} \Lambda_j - u_n) \Lambda_m(\boldsymbol{r}') \rangle = \langle \mathcal{L}_{nj} \Lambda_j \Lambda_m(\boldsymbol{r}') \rangle - \langle u_n \Lambda_m(\boldsymbol{r}') \rangle = 0. \tag{B8}$$

According to the linear property of $\mathcal{L}_{nj}$, finally we get

$$\mathcal{L}_{nj} \langle \Lambda_j \Lambda_m(\boldsymbol{r}') \rangle = \langle u_n \Lambda_m(\boldsymbol{r}') \rangle. \tag{B9}$$

Equation (B9) is equivalent to (4.4) in the article by replacing the free index n with i. What is noteworthy is that the equation holds for all possible $\Lambda_m(\boldsymbol{r}')$, $m = 1, 2, 3$; $\boldsymbol{r}' \in \Omega$, a number which is large enough to determine $\mathcal{L}_{nj}$.

Appendix C. A procedure card for the FFT implementation of FLSE

I. Calculate R_{jm} and q_{im} by

$$R_{jm}(x_a, y_b, z''_{c''}; z'_{c'}) = \langle \Lambda_j(x_a, y_b, z''_{c''}) \Lambda_m(0, 0, z'_{c'}) \rangle, \tag{C1}$$

$$q_{im}(x_a, y_b, z_c; z'_{c'}) = \langle u_i(x_a, y_b, z_c) \Lambda_m(0, 0, z'_{c'}) \rangle. \tag{C2}$$

II. Perform 2-D windowed FFT on R_{jm} and q_{im}, i.e.

$$\tilde{R}_{jm}(k_\alpha, k_\beta, z''_{c''}; z'_{c'}) = FFT2D\{R_{jm}(x_a, y_b, z''_{c''}; z'_{c'})\}, \tag{C3}$$

$$\tilde{q}_{im}(k_\alpha, k_\beta, z_c; z'_{c'}) = FFT2D\{q_{im}(x_a, y_b, z_c; z'_{c'})\}. \tag{C4}$$

III. Arrange $\tilde{R}_{jm}(k_\alpha, k_\beta, z''_{c''}; z'_{c'})$ and $\tilde{q}_{im}(k_\alpha, k_\beta, z_c; z'_{c'})$ into matrix $\mathbf{A}^{\alpha,\beta}$ and vector $\mathbf{b}^{i,\alpha,\beta,c}$, such as

$$\mathbf{A}^{\alpha,\beta}|_{c'+(m-1)\times Nz, c''+(j-1)\times Nz} = \tilde{R}_{jm}(k_\alpha, k_\beta, z''_{c''}; z'_{c'}), \tag{C5}$$

$$\mathbf{b}^{i,\alpha,\beta,c}|_{c'+(m-1)\times Nz} = \tilde{q}_{im}(k_\alpha, k_\beta, z_c; z'_{c'}); \tag{C6}$$

note that the vertical line indicates extracting the element from the left matrix or vector according to the prescribed index on the right-lower corner.

IV. For any i, α, β, c, solve $(\mathbf{A}^{\alpha,\beta} + s\tilde{\delta}(k_\alpha, k_\beta)\mathbf{I})\boldsymbol{\varphi}^{i,\alpha,\beta,c} = \mathbf{b}^{i,\alpha,\beta,c}$, where

$$\tilde{\delta}(k_\alpha, k_\beta) = FFT2D\{\delta(x_a, y_b)\}, \tag{C7}$$

and

$$\delta(x_a, y_b) = \begin{cases} 1 & \text{if } x_a = 0, \ y_b = 0 \\ 0 & \text{otherwise} \end{cases}. \tag{C8}$$

V. Collect all the solution $\boldsymbol{\varphi}^{i,\alpha,\beta,c}$ to get $\tilde{\varphi}_{ij}(k_\alpha, k_\beta, z_c; z''_{c''})$, i.e.

$$\tilde{\varphi}_{ij}(k_\alpha, k_\beta, z_c; z''_{c''}) = \boldsymbol{\varphi}^{i,\alpha,\beta,c}|_{c''+(j-1)\times Nz}. \tag{C9}$$

VI. Perform 2-D inverse FFT on $\tilde{\varphi}_{ij}(k_\alpha, k_\beta, z_c; z''_{c''})$ and return $\varphi_{ij}(x_a, y_b, z_c; z''_{c''})$, i.e.

$$\varphi_{ij}(x_a, y_b, z_c; z''_{c''}) = IFFT2D\{\tilde{\varphi}_{ij}(k_\alpha, k_\beta, z_c; z''_{c''})\}. \tag{C10}$$

REFERENCES

ADRIAN, R.J. 1994 Stochastic estimation of conditional structure: a review. *Flow Turbul. Combust.* **53** (3), 291–303.

ADRIAN, R.J. 2007 Hairpin vortex organization in wall turbulence. *Phys. Fluids* **19** (4), 041301.

ADRIAN, R.J., MEINHART, C.D. & TOMKINS, C.D. 2000 Vortex organization in the outer region of the turbulent boundary layer. *J. Fluid Mech.* **422**, 1–54.

DEL ÁLAMO, J.C., JIMÉNEZ, J., ZANDONADE, P. & MOSER, R.D. 2006 Self-similar vortex clusters in the turbulent logarithmic region. *J. Fluid Mech.* **561**, 329–358.

BAARS, W.J., HUTCHINS, N. & MARUSIC, I. 2016 Spectral stochastic estimation of high-Reynolds-number wall-bounded turbulence for a refined inner-outer interaction model. *Phys. Rev. Fluids* **1**, 054406.

BAARS, W.J. & MARUSIC, I. 2020a Data-driven decomposition of the streamwise turbulence kinetic energy in boundary layers. Part 1. Energy spectra. *J. Fluid Mech.* **882**, A25.

BAARS, W.J. & MARUSIC, I. 2020b Data-driven decomposition of the streamwise turbulence kinetic energy in boundary layers. Part 2. Integrated energy and A1. *J. Fluid Mech.* **882**, A26.

BANDYOPADHYAY, P. 1980 Large structure with a characteristic upstream interface in turbulent boundary layers. *Phys. Fluids* **23** (11), 2326–2327.

BANDYOPADHYAY, P.R. 1989 Effect of abrupt pressure gradients on the structure of turbulent boundary layers. In *Proceedings of the 10th Australasian Fluid Mechanics Conference* (ed. A.E. Perry *et al.*), vol. 1, pp. 1.1–1.4. University of Melbourne.

BANDYOPADHYAY, P.R. 2020 Vortex bursting near a free surface. *J. Fluid Mech.* **888**, A27.

BANDYOPADHYAY, P.R. & HELLUM, A.M. 2014 Modeling how shark and dolphin skin patterns control transitional wall-turbulence vorticity patterns using spatiotemporal phase reset mechanisms. *Sci. Rep.* **4** (1), 6650.

BANDYOPADHYAY, P.R. & WATSON, R.D. 1988 Structure of rough-wall turbulent boundary layers. *Phys. Fluids* **31** (7), 1877–1883.

BATCHELOR, G.K. 1967 *An Introduction to Fluid Mechanics*. Cambridge University Press.

BERK, T. & GANAPATHISUBRAMANI, B. 2019 Effects of vortex-induced velocity on the development of a synthetic jet issuing into a turbulent boundary layer. *J. Fluid Mech.* **870**, 651–679.

BERNARD, P.S. 2013 Vortex dynamics in transitional and turbulent boundary layers. *AIAA J.* **51** (8), 1828–1842.

BERNARD, P.S., THOMAS, J.M. & HANDLER, R.A. 1993 Vortex dynamics and the production of Reynolds stress. *J. Fluid Mech.* **253**, 385–419.

BORRELL, G., SILLERO, J.A. & JIMÉNEZ, J. 2013 A code for direct numerical simulation of turbulent boundary layers at high Reynolds numbers in BG/P supercomputers. *Comput. Fluids* **80**, 37–43.

BRADSHAW, P. 1967 The turbulence structure of equilibrium boundary layers. *J. Fluid Mech.* **29** (4), 625–645.

CAPRACE, D.-G., WINCKELMANS, G. & CHATELAIN, P. 2020 An immersed lifting and dragging line model for the vortex particle-mesh method. *Theor. Comput. Fluid Dyn.* **34** (1–2), 21–48.

CHAKRABORTY, P., BALACHANDAR, S. & ADRIAN, R.J. 2005 On the relationships between local vortex identification schemes. *J. Fluid Mech.* **535** (4), 189–214.

CHEN, X. & SREENIVASAN, K.R. 2021 Reynolds number scaling of the peak turbulence intensity in wall flows. *J. Fluid Mech.* **908**, R3.

CHONG, M.S., PERRY, A.E. & CANTWELL, B.J. 1990 A general classification of three-dimensional flow fields. *Phys. Fluids* **2** (5), 765–777.

CHRISTENSEN, K.T. & ADRIAN, R.J. 2001 Statistical evidence of hairpin vortex packets in wall turbulence. *J. Fluid Mech.* **431**, 433–443.

CORRSIN, S. 1962 Turbulent dissipation fluctuations. *Phys. Fluids* **5** (10), 1301.

DAS, S.K., TANAHASHI, M., SHOJI, K. & MIYAUCHI, T. 2006 Statistical properties of coherent fine eddies in wall-bounded turbulent flows by direct numerical simulation. *Theor. Comput. Fluid Dyn.* **20** (2), 55–71.

DENG, S., PAN, C., WANG, J. & HE, G. 2018 On the spatial organization of hairpin packets in a turbulent boundary layer at low-to-moderate Reynolds number. *J. Fluid Mech.* **844**, 635–668.

EINSTEIN, H.A. & LI, H. 1958 The viscous sublayer along a smooth boundary. *Trans. Am. Soc. Civil Engrs* **123**, 293–313.

FERNHOLZ, H.H. & FINLEYT, P.J. 1996 The incompressible zero-pressure-gradient turbulent boundary layer: an assessment of the data. *Prog. Aerosp. Sci.* **32** (4), 245–311.

GAD-EL-HAK, M. & BANDYOPADHYAY, P.R. 1994 Reynolds number effects in wall-bounded turbulent flows. *Appl. Mech. Rev.* **47** (8), 307–365.

GANAPATHISUBRAMANI, B., LONGMIRE, E.K. & MARUSIC, I. 2003 Characteristics of vortex packets in turbulent boundary layers. *J. Fluid Mech.* **478**, 35–46.

GANAPATHISUBRAMANI, B., LONGMIRE, E.K. & MARUSIC, I. 2006 Experimental investigation of vortex properties in a turbulent boundary layer. *Phys. Fluids* **18** (5), 1–464.

GAO, Q., ORTIZ-DUEÑAS, C. & LONGMIRE, E.K. 2007 Circulation signature of vortical structures in turbulent boundary layers. In *16th Australasian Fluid Mechanics Conference Crown Plaza, Gold Coast, Australia*.

GAO, Q., ORTIZ-DUEÑAS, C. & LONGMIRE, E.K. 2011 Analysis of vortex populations in turbulent wall-bounded flows. *J. Fluid Mech.* **678** (8), 87–123.

GAO, Y. & LIU, C. 2018 Rortex and comparison with eigenvalue-based vortex identification criteria. *Phys. Fluids* **30**, 085107.

GENTLE, J.E. 1998 *Numerical Linear Algebra for Applications in Statistics*. Springer.

HAMA, F. 1954 Boundary layer characteristics for smooth and rough surfaces. In *Trans. 1954 Annual Meeting of the Society of Naval Architects and Marine Engineers*. SNAME.

HAMBLETON, W.T., HUTCHINS, N. & MARUSIC, I. 2006 Simultaneous orthogonal-plane particle image velocimetry measurements in a turbulent boundary layer. *J. Fluid Mech.* **560** (560), 53–64.

HEAD, M.R. & BANDYOPADHYAY, P. 1981 New aspects of turbulent boundary-layer structure. *J. Fluid Mech.* **107** (107), 297–338.

HERPIN, S., STANISLAS, M., JEAN, M.F. & COUDERT, S. 2013 Influence of the Reynolds number on the vortical structures in the logarithmic region of turbulent boundary layers. *J. Fluid Mech.* **716** (2), 5–50.

HU, R., YANG, X.I.A. & ZHENG, X. 2020 Wall-attached and wall-detached eddies in wall-bounded turbulent flows. *J. Fluid Mech.* **885**, A30.

HUNT, J.C.R., WRAY, A.A. & MOIN, P. 1988 Eddies, streams, and convergence zones in turbulent flows. *Report No.* CTR-S88, pp. 193–208. Center for Turbulence Research.

HUTCHINS, N., HAMBLETON, W.T. & MARUSIC, I. 2005 Inclined cross-stream stereo particle image velocimetry measurements in turbulent boundary layers. *J. Fluid Mech.* **541**, 21–54.

HUTCHINS, N. & MARUSIC, I. 2007 Large-scale influences in near-wall turbulence. *Phil. Trans. R. Soc. Lond.* A **365** (1852), 647–664.

JEONG, J.J.J. & HUSSAIN, F. 1995 On the identification of a vortex. *J. Fluid Mech.* **332** (1), 339–363.

JIMÉNEZ, J. & PINELLI, A. 1999 The autonomous cycle of near-wall turbulence. *J. Fluid Mech.* **389** (389), 335–359.

JIMÉNEZ, J., WRAY, A.A., SAFFMAN, P.G. & ROGALLO, R.S. 1993 The structure of intense vorticity in isotropic turbulence. *J. Fluid Mech.* **255**, 65–90.

JODAI, Y. & ELSINGA, G.E. 2016 Experimental observation of hairpin auto-generation events in a turbulent boundary layer. *J. Fluid Mech.* **795**, 611–633.

KANG, S.J., TANAHASHI, M. & MIYAUCHI, T. 2007 Dynamics of fine scale eddy clusters in turbulent channel flows. *J. Turbul.* **8**, N52.

KLINE, S.J., REYNOLDS, W.C., SCHRAUB, F.A. & RUNSTADLER, P.W. 1967 The structure of turbulent boundary layers. *J. Fluid Mech.* **30** (4), 741–773.

KOUMOUTSAKOS, P. & LEONARD, A. 1995 High-resolution simulations of the flow around an impulsively started cylinder using vortex methods. *J. Fluid Mech.* **296** (1), 1–38.

KRESS, R. 2014 *Tikhonov Regularization*, pp. 323–349. Springer.

KUO, A.Y.-S. & CORRSIN, S. 1972 Experiment on the geometry of the fine-structure regions in fully turbulent fluid. *J. Fluid Mech.* **56** (3), 447–479.

LEE, J., LEE, J., CHOI, J. & SUNG, H. 2014 Spatial organization of large- and very-large-scale motions in a turbulent channel flow. *J. Fluid Mech.* **749**, 818–840.

LEE, J.-H. & SUNG, H.J. 2009 Structures in turbulent boundary layers subjected to adverse pressure gradients. *J. Fluid Mech.* **639**, 101–131.

LEONARD, A. 1985 Computing three-dimensional incompressible flows with vortex elements. *Annu. Rev. Fluid Mech.* **17** (1), 523–559.

LOZANO-DURÁN, A. & JIMÉNEZ, J. 2014 Time-resolved evolution of coherent structures in turbulent channels: characterization of eddies and cascades. *J. Fluid Mech.* **759**, 432–471.

LUND, T.S., WU, X. & SQUIRES, K.D. 1998 Generation of turbulent inflow data for spatially-developing boundary layer simulations. *J. Comput. Phys.* **140** (2), 233–258.

LUNDGREN, T.S. 1982 Strained spiral vortex model for turbulent fine structure. *Phys. Fluids* **25** (12), 2193–2203.

MARUSIC, I. 2001 On the role of large-scale structures in wall turbulence. *Phys. Fluids* **13** (13), 735–743.

MARUSIC, I. & ADRIAN, R.J. 2012 The eddies and scales of wall turbulence. In *Turbulence* (ed. K.R. Sreenivasan, P.A. Davidson & Y. Kaneda), pp. 176–220. Cambridge University Press.

MARUSIC, I., BAARS, W.J. & HUTCHINS, N. 2017 Scaling of the streamwise turbulence intensity in the context of inner-outer interactions in wall turbulence. *Phys. Rev. Fluids* **2**, 100502.

MARUSIC, I., MATHIS, R. & HUTCHINS, N. 2010 Predictive model for wall-bounded turbulent flow. *Science* **329** (5988), 193–196.

MARUSIC, I. & MONTY, J.P. 2019 Attached eddy model of wall turbulence. *Annu. Rev. Fluid Mech.* **51**, 49–74.

MARUSIC, I. & PERRY, A.E. 1995 A wall-wake model for the turbulence structure of boundary layers. Part 2. Further experimental support. *J. Fluid Mech.* **298** (298), 389–407.

MATHIS, R., HUTCHINS, N. & MARUSIC, I. 2011 A predictive inner–outer model for streamwise turbulence statistics in wall-bounded flows. *J. Fluid Mech.* **681**, 537–566.

MONKEWITZ, P.A., CHAUHAN, K.A. & NAGIB, H.M. 2007 Self-consistent high-Reynolds-number asymptotics for zero-pressure-gradient turbulent boundary layers. *Phys. Fluids* **19** (11), 319–316.

NATRAJAN, V.K., WU, Y. & CHRISTENSEN, K.T. 2007 Spatial signatures of retrograde spanwise vortices in wall turbulence. *J. Fluid Mech.* **574**, 155–167.

ONG, L. & WALLACE, J.M. 1998 Joint probability density analysis of the structure and dynamics of the vorticity field of a turbulent boundary layer. *J. Fluid Mech.* **367** (367), 291–328.

PANTON, R.L. 2001 Overview of the self-sustaining mechanisms of wall turbulence. *Prog. Aerosp. Sci.* **37** (4), 341–383.

PERRY, A.E. & CHONG, M.S. 1982 On the mechanism of wall turbulence. *J. Fluid Mech.* **119**, 173–217.

PERRY, A.E. & CHONG, M.S. 1987 A description of eddying motions and flow patterns using critical-point concepts. *Annu. Rev. Fluid Mech.* **19** (1), 125–155.

PERRY, A.E., HENBEST, S. & CHONG, M.S. 1986 A theoretical and experimental study of wall turbulence. *J. Fluid Mech.* **165**(165), 163–199.

PERRY, A.E. & MARUSIC, I. 1995 A wall-wake model for the turbulence structure of boundary layers. Part 1. Extension of the attached eddy hypothesis. *J. Fluid Mech.* **298** (298), 361–388.

PIROZZOLI, S., BERNARDINI, M. & GRASSO, F. 2010 On the dynamical relevance of coherent vortical structures in turbulent boundary layers. *J. Fluid Mech.* **648**, 325–349.

PULLIN, D.I. & SAFFMAN, P.G. 1993 On the Lundgren–Townsend model of turbulent fine scales. *Phys. Fluids* **5** (1), 126–145.

RAMIREZ, D., VIA, J. & SANTAMARIA, I. 2008 A generalization of the magnitude squared coherence spectrum for more than two signals: definition, properties and estimation. In *Proceedings of the IEEE International Conference on Acoustics, Speech, and Signal Processing (ICASSP), Las Vegas, Nevada, USA.*

SCHOPPA, W. & HUSSAIN, F. 2002 Coherent structure generation in near-wall turbulence. *J. Fluid Mech.* **453**, 57–108.

SILLERO, J.A., JIMÉNEZ, J. & MOSER, R.D. 2013 One-point statistics for turbulent wall-bounded flows at Reynolds numbers up to $\delta^+ \approx 2000$. *Phys. Fluids* **25** (10), 105102.

SILLERO, J.A., JIMÉNEZ, J. & MOSER, R.D. 2014 Two-point statistics for turbulent boundary layers and channels at Reynolds numbers up to $\delta^+ \approx 2000$. *Phys. Fluids* **26** (10), 105109.

DE SILVA, C.M., HUTCHINS, N. & MARUSIC, I. 2016*a* Uniform momentum zones in turbulent boundary layers. *J. Fluid Mech.* **786**, 309–331.

DE SILVA, C.M., KEVIN, A.K., BAIDYA, R., HUTCHINS, N. & MARUSIC, I. 2018 Large coherence of spanwise velocity in turbulent boundary layers. *J. Fluid Mech.* **847**, 161–185.

DE SILVA, C.M., WOODCOCK, J.D., HUTCHINS, N. & MARUSIC, I. 2016*b* Influence of spatial exclusion on the statistical behavior of attached eddies. *Phys. Rev. Fluids* **1**, 022401.

SIMENS, M.P., JIMÉNEZ, J., HOYAS, S. & MIZUNO, Y. 2009 A high-resolution code for turbulent boundary layers. *J. Comput. Phys.* **228** (11), 4218–4231.

STANISLAS, M., PERRET, L. & FOUCAUT, J.M. 2008 Vortical structures in the turbulent boundary layer: a possible route to a universal representation. *J. Fluid Mech.* **602**, 327–382.

STOICA, P. & MOSES, R. 2005 *Spectral Analysis of Signals.* Prentice Hall.

SYNGE, J.L. & LIN, C.C. 1943 On a statistical model of isotropic turbulence. *Trans. R. Soc. Can.* **37**, 45.

TANAHASHI, M., KANG, S.J., MIYAMOTO, T., SHIOKAWA, S. & MIYAUCHI, T. 2004 Scaling law of fine scale eddies in turbulent channel flows up to $Re_\tau = 800$. *Intl J. Heat Fluid Flow* **25** (3), 331–340.

TENNEKES, H. 1968 Simple model for the small-scale structure of turbulence. *Phys. Fluids* **11** (3), 669–671.

THEODORSEN, T. 1952 Mechanism of turbulence. In *Proceedings of the Midwestern Conference on Fluid Mechanics*, Ohio State University.

TIAN, S., GAO, Y., DONG, X. & LIU, C. 2018 Definitions of vortex vector and vortex. *J. Fluid Mech.* **849**, 312–339.

TINNEY, C.E., COIFFET, F., DELVILLE, J., HALL, A.M., JORDAN, P. & GLAUSER, M.N. 2006 On spectral linear stochastic estimation. *Exp. Fluids* **41** (5), 763–775.

TOWNSEND, A.A. 1951 On the fine-scale structure of turbulence. *Proc. R. Soc. Lond.* **208** (1095), 534–542.

TOWNSEND, A.A. 1956 The structure of turbulent shear flow. *Q. J. R. Meteorol. Soc.* **83** (357), 411–412.

WANG, C., GAO, Q., WANG, J., WANG, B. & PAN, C. 2019 Experimental study on dominant vortex structures in near-wall region of turbulent boundary layer based on tomographic particle image velocimetry. *J. Fluid Mech.* **874**, 426–454.

WANG, W., PAN, C., GAO, Q. & WANG, J. 2018 Wall-normal variation of spanwise streak spacing in turbulent boundary layer with low-to-moderate Reynolds number. *Entropy* **21** (1), 24.

WANG, W., PAN, C. & WANG, J. 2021 Energy transfer structures associated with large-scale motions in a turbulent boundary layer. *J. Fluid Mech.* **906**, A14.

WANG, H.P., WANG, S.Z. & HE, G.W. 2017 The spanwise spectra in wall-bounded turbulence. *Acta Mech. Sinica* **34** (3), 452–461.

WOODCOCK, J.D. & MARUSIC, I. 2015 The statistical behaviour of attached eddies. *Phys. Fluids* **27** (1), 97–120.

WU, Y. & CHRISTENSEN, K.T. 2006 Population trends of spanwise vortices in wall turbulence. *J. Fluid Mech.* **568**, 55–76.

XIONG, S. & YANG, Y. 2019 Identifying the tangle of vortex tubes in homogeneous isotropic turbulence. *J. Fluid Mech.* **874**, 952–978.

YANG, X.I.A., MARUSIC, I. & MENEVEAU, C. 2016 Moment generating functions and scaling laws in the inertial layer of turbulent wall-bounded flows. *J. Fluid Mech.* **791**, R2.

YOON, M., HWANG, J., YANG, J. & SUNG, H.J. 2020 Wall-attached structures of streamwise velocity fluctuations in an adverse-pressure-gradient turbulent boundary layer. *J. Fluid Mech.* **885**, A12.

ZHOU, J. 1997 Self-sustaining formation of packets of hairpin vortices in a turbulent wall layer. PhD thesis, University of Illinois.

ZHOU, J., ADRIAN, R.J., BALACHANDAR, S. & KENDALL, T.M. 1999 Mechanisms for generating coherent packets of hairpin vortices in channel flow. *J. Fluid Mech.* **387**, 353–396.

ZHU, L. & XI, L. 2019 Vortex axis tracking by iterative propagation (VATIP): a method for analysing three-dimensional turbulent structures. *J. Fluid Mech.* **866**, 169–215.